

RESEARCH ARTICLE

NEURODEGENERATION

Pharmacological modulation of septins restores calcium homeostasis and is neuroprotective in models of Alzheimer's disease

Katrien Princen^{1†}, Tom Van Dooren^{1††}, Marit van Gorse¹, Nikolaos Louros^{2,3§¶}, Xiaojuan Yang⁴, Michael Dumbacher¹, Ilse Bastiaens¹, Kristel Coupet¹, Shana Dupont¹, Eva Cuveliers¹, Annick Lauwers¹, Mohamed Laghmouchi¹, Thomas Vanwelden¹, Sofie Carmans¹, Nele Van Damme¹, Hein Duhamel¹, Seppe Vansteenkiste¹, Jovan Prerad¹, Karolien Pipeleers¹, Olivier Rodiers¹, Liese De Ridder¹, Sofie Claes¹, Yoni Busschots¹, Lentel Pringels¹, Vanessa Verhelst¹, Eveline Debroux¹, Marinka Brouwer⁵, Sam Lievens^{6,7#}, Jan Tavernier^{6,7#}, Melissa Farinelli⁸, Sandrine Hughes-Asceri⁸, Marieke Voets¹, Joris Winderickx^{1,9}, Stefaan Wera^{1,10}, Joris de Wit⁵, Joost Schymkowitz^{2,3}, Frederic Rousseau^{2,3}, Henrik Zetterberg^{11,12,13,14,15,16}, Jeffrey L. Cummings¹⁷, Wim Annaert⁴, Tom Cornelissen¹, Hans De Winter¹⁸, Koen De Witte¹, Marc Fivaz^{1*}, Gerard Griffioen^{1*}

Abnormal calcium signaling is a central pathological component of Alzheimer's disease (AD). Here, we describe the identification of a class of compounds called ReS19-T, which are able to restore calcium homeostasis in cell-based models of tau pathology. Aberrant tau accumulation leads to uncontrolled activation of store-operated calcium channels (SOCs) by remodeling septin filaments at the cell cortex. Binding of ReS19-T to septins restores filament assembly in the disease state and restrains calcium entry through SOCs. In amyloid- β and tau-driven mouse models of disease, ReS19-T agents restored synaptic plasticity, normalized brain network activity, and attenuated the development of both amyloid- β and tau pathology. Our findings identify the septin cytoskeleton as a potential therapeutic target for the development of disease-modifying AD treatments.

Alzheimer's disease (AD) is the main cause of dementia, afflicting >50 million people worldwide (1). With no cure and few approved therapies, AD is fast becoming one of the most expensive and devastating diseases of this century. Therefore, there is an urgent need to accelerate the development of therapeutics that target the root cause of neurodegeneration in AD.

Deranged calcium signaling is increasingly recognized as a central pathological event in AD and other types of dementia. Sustained disturbances in calcium signaling occur in the preclinical phase of the disease, before the development of overt symptoms (2–5), and trigger synapse disruption (6, 7), a key pathological event that underlies memory impair-

ment and precedes neuronal death (8). Calcium dysregulation in AD is multidimensional and complex, but ultimately manifests with sustained elevation of cytoplasmic calcium concentration $[Ca^{2+}]_{cyto}$ in both familial and idiopathic forms of the disease (9, 10).

In diseased neurons, elevated resting $[Ca^{2+}]_{cyto}$ contributes to the development of AD pathology, including the production of pathological amyloid- β (A β) and tau species (11–14). Reciprocally, AD pathological changes cause an elevation in resting $[Ca^{2+}]_{cyto}$, which triggers a program of neurodegeneration initiated by synaptic disruption and culminating with the activation of neuronal death pathways (15–18). This suggests that deregulated $[Ca^{2+}]_{cyto}$ fuels a self-reinforcing amplification of AD

pathobiology, ultimately causing neuronal demise.

A variety of calcium channels and signaling systems have been shown to be altered in AD, ranging from increased activity of *N*-methyl-D-aspartate (NMDA) receptors (19) and voltage-gated calcium channels (VGCCs) (20) at the synapse to impaired mitochondrial calcium buffering (21) and exaggerated calcium release from the endoplasmic reticulum (ER), an effect mediated by up-regulation of inositol-3-phosphate (22) and ryanodine (6) receptors. Linked to disturbances in ER calcium homeostasis is store-operated calcium entry (SOCE), a calcium influx pathway activated by depletion of calcium from ER stores. SOCE is down-regulated by several familial AD mutations in presenilin-1 (PS1) but stimulated by others, depending on the impact of these mutations on ER calcium leakage (10). Moreover, an excess of tau exacerbates SOCE (23), and this calcium influx pathway promotes the activation of the inflammasome in diseased microglial cells (24), suggesting a context-specific influence of SOCE in AD.

These observations indicate that calcium dysfunction in AD is a promising therapeutic target. However, interfering with physiological calcium signaling events is likely to have adverse consequences on synaptic networks and cognitive performance and may affect non-neurologic organ systems, including the heart. Here, we report the identification and characterization of a class of compounds called ReS19-T that circumvent this problem by selectively targeting an aberrant form of SOCE triggered by pathological tau without affecting synaptic- and receptor-mediated Ca^{2+} signaling in physiological conditions. ReS19-T compounds efficiently crossed the blood–brain barrier, rescued synaptic and cognitive deficits in AD mouse models, and reduced A β and tau pathology.

ReS19-T: A small-molecule scaffold that restores calcium homeostasis and neutralizes tau- and A β -driven neurotoxicity

To identify potential AD drug targets and corresponding therapeutics, we developed a

¹reMYND NV, Bio-Incubator, 3001 Leuven-Heverlee, Belgium. ²Switch Laboratory, VIB Center for Brain and Disease Research, 3000 Leuven, Belgium. ³Switch Laboratory, Department of Cellular and Molecular Medicine, KU Leuven, 3000 Leuven, Belgium. ⁴Laboratory for Membrane Trafficking, VIB-Center for Brain and Disease Research and Department of Neurosciences, Leuven Brain Institute, 3000 Leuven, Belgium. ⁵Laboratory of Synapse Biology, VIB Center for Brain & Disease Research and KU Leuven Department of Neurosciences, Leuven Brain Institute, 3000 Leuven, Belgium. ⁶Cytokine Receptor Lab, VIB Center for Medical Biotechnology, 9052 Ghent, Belgium. ⁷Department of Biomolecular Medicine, Ghent University, 9000 Ghent, Belgium. ⁸E-PHY-SCIENCE, Bioparc Sophia-Antipolis, 06410 Biot, France. ⁹Functional Biology, Department of Biology, KU Leuven, 3001 Leuven-Heverlee, Belgium. ¹⁰ViroVet NV, 3001 Leuven-Heverlee, Belgium. ¹¹Department of Psychiatry and Neurochemistry, Institute of Neuroscience and Physiology, the Sahlgrenska Academy at the University of Gothenburg, S-431 80 Mölndal, Sweden. ¹²Clinical Neurochemistry Laboratory, Sahlgrenska University Hospital, S-431 80 Mölndal, Sweden. ¹³Department of Neurodegenerative Disease, UCL Queen Square Institute of Neurology, London WC1N 3BG, UK. ¹⁴UK Dementia Research Institute at UCL, London WC1E 6BT, UK. ¹⁵Hong Kong Center for Neurodegenerative Diseases, Clear Water Bay, Hong Kong, China. ¹⁶Wisconsin Alzheimer's Disease Research Center, University of Wisconsin School of Medicine and Public Health, University of Wisconsin-Madison, Madison, WI 53792, USA. ¹⁷Chambers-Grundy Center for Transformative Neuroscience, Department of Brain Health, School of Integrated Health Sciences, University of Nevada, Las Vegas, Las Vegas, NV 89154, USA. ¹⁸Laboratory of Medicinal Chemistry, Department of Pharmaceutical Sciences, University of Antwerp, 2610 Wilrijk, Belgium.

*Corresponding author. Email: marc.fivaz@remynd.com (M.F.); gerard.griffioen@ext.remynd.com (G.G.)

†These authors contributed equally to this work.

‡Present address: UCB Biopharma SRL, B-1420 Braine-l'Alleud, Belgium.

§Present address: Center for Alzheimer's and Neurodegenerative Diseases, Peter O'Donnell Jr. Brain Institute, University of Texas Southwestern Medical Center, Dallas, TX, 75390, USA.

¶Present address: Department of Biophysics, University of Texas Southwestern Medical Center, Dallas, TX, 75390, USA.

#Present address: Orionis Biosciences, 9052 Ghent, Belgium.

cell-based screening assay that recapitulates tau- and Ca^{2+} -induced toxicity in human neuroblastoma cells (25). This assay involves stable expression of human tau with a pathological mutation (P301L) associated with frontotemporal dementia (FTD) and causing aggressive tau hyperphosphorylation and aggregation (26), in combination with chronic exposure to all-trans retinoic acid (ATRA), an inducer of neuronal differentiation. In this context, tauP301L causes extensive cell death compared with wild-type (WT) tau or no transgene expression (fig. S1A). Previous characterization of this assay revealed that toxicity is associated with elevation of cytoplasmic calcium $[\text{Ca}^{2+}]_{\text{cyto}}$, and that interventions lowering $[\text{Ca}^{2+}]_{\text{cyto}}$ efficiently rescue cell death, indicating calcium-driven tau neurotoxicity (25).

Screening of an in-house compound library led to the identification of several hits that alleviate $[\text{Ca}^{2+}]_{\text{cyto}}$ overload and toxicity. We focused on a thiaziazole derivative for further development. After multiple rounds of structure-activity optimization, we obtained a series of compounds with a common scaffold, ReS19-T, that efficiently counteract toxicity and restore normal $[\text{Ca}^{2+}]_{\text{cyto}}$. An estate of closely related ReS19-T compounds, REM0046127 (REM127), REM0046123 (REM123), and REM0044929 (REM929), with nanomolar potencies were used in the experiments presented here (Fig. 1A and figs. S1B and S2D). REM127, the most potent compound of this chemical series, reduced toxicity and $[\text{Ca}^{2+}]_{\text{cyto}}$ with median effective concentrations ($\text{EC}_{50\text{s}}$) of 15 and 19 nM, respectively (Fig. 1A) but had no effect on tau

expression or ATRA-dependent gene transcription (fig. S1, C and D). Neurotoxic soluble amyloid oligomers ($\text{A}\beta$ -derived diffusible ligands, ADDLs) induce tau hyperphosphorylation and a sustained increase in neuronal $[\text{Ca}^{2+}]_{\text{cyto}}$ (27–29). To test whether REM127 rescues ADDL-induced synaptic loss and neuronal toxicity, we treated rat hippocampal neurons with purified ADDLs in the presence of compound or vehicle. REM127 restored dendritic spine density (Fig. 1, B and C) and fully rescued neurons from ADDL-induced cell death (Fig. 1D), demonstrating that both tau- and $\text{A}\beta$ -induced neurotoxicity are countered by REM127 in cell-based assays.

Septin 6 is a high-affinity target of ReS19-T

To identify ReS19-T targets, we performed a three-hybrid screen in mammalian cells (30).

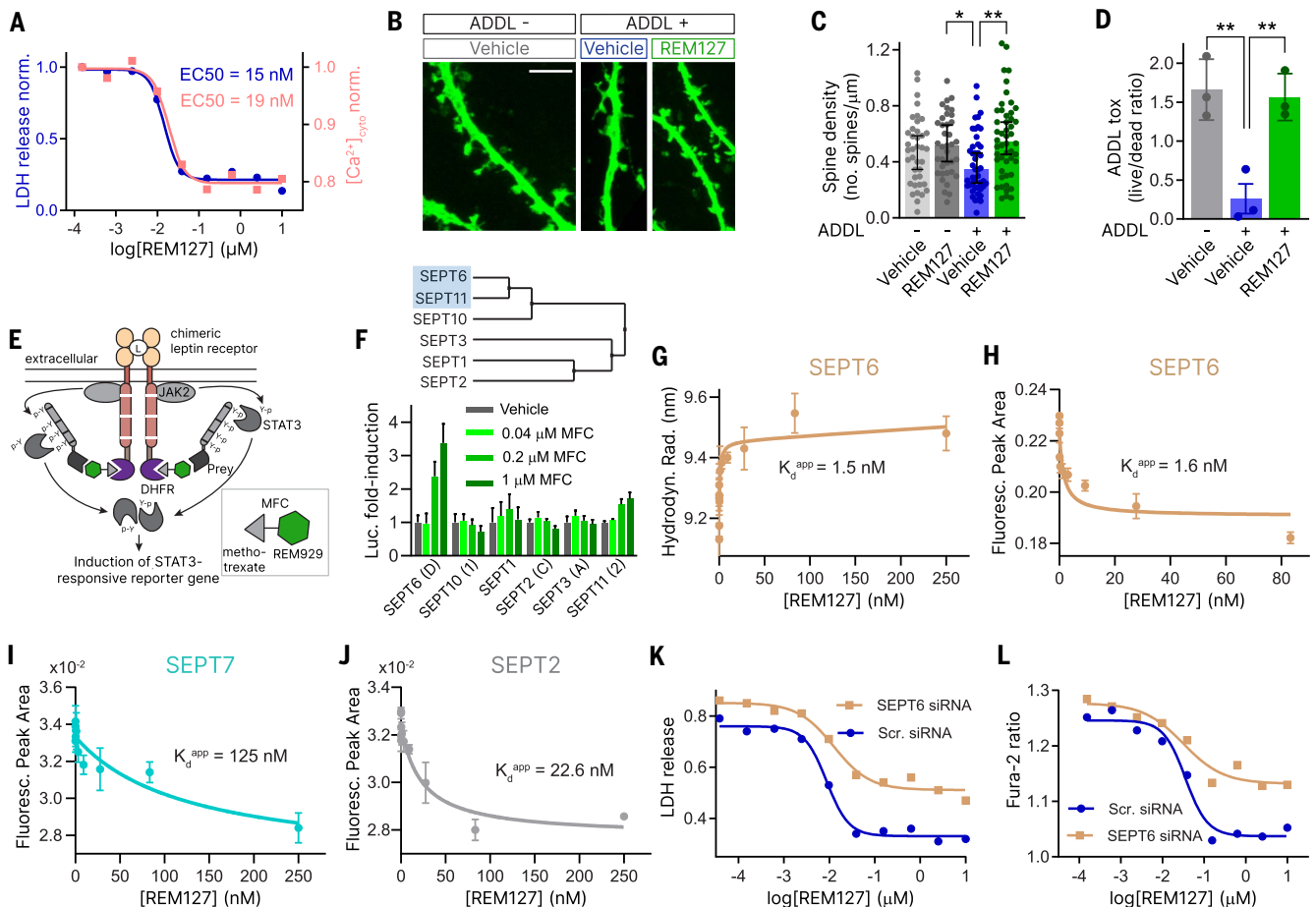


Fig. 1. Identification of ReS19-T and its high-affinity target. (A) Cell death and $[\text{Ca}^{2+}]_{\text{cyto}}$ in ATRA-treated tauP301L-expressing BE(2)-M17 cells in presence of increasing concentrations of REM127. (B to D) Rat hippocampal neurons [22 days in vitro (DIV)] treated with vehicle or REM127 (240 nM) and exposed or not to ADDL (0.5 μM) [(B) and (C)] or ADDL (1 μM) (D) for 24 hours. (B and C) Dendritic spine density measured in dendritic segments of Marcks-GFP-transfected neurons. ADDL-/Veh, $N = 39$; ADDL-/REM127, $N = 37$; ADDL+/Veh, $N = 43$; and ADDL+/REM127, $N = 50$. Scale bar, 5 μm . Error bars indicate 95% confidence interval (CI). (D) ADDL-induced cell death in neurons exposed to the indicated treatments ($N = 3$). Error bars indicate SD. (E) Three-hybrid screen

approach to identifying ReS19-T-interacting proteins. (F) In cellulo interaction of MFC (REM929 linked to methotrexate) with different septin isoforms ($N = 3$, error bars indicate SD). Inset shows phylogenetic analysis of septin isoforms probed in the three-hybrid assay. (G to J) FIDA binding isotherms of REM127 to human SEPT6, SEPT7, and SEPT2. Error bars indicate SD. (K and L) Effects of scrambled (scr) and SEPT6-lowering siRNAs on REM127-induced relief of toxicity (K) and $[\text{Ca}^{2+}]_{\text{cyto}}$ overload (L) in ATRA-treated tauP301L-expressing BE(2)-M17 cells. * $P < 0.05$, ** $P < 0.01$, Kruskal-Wallis with Dunn's multiple-comparisons tests for (C) and one-way ANOVA with multiple pairwise comparisons of means (Tukey's test) for (D). See also corresponding figs. S1 to S3.

As “prey,” we used a genome-wide collection of human open reading frames (ORFs) fused to truncated gp130, and as “bait,” we used REM929 linked to methotrexate (MFC). Interaction of MFC with a prey should complement a signaling-deficient leptin receptor and induce a STAT3-responsive reporter gene (Fig. 1E). Only three cDNAs elicited at least a twofold induction of the reporter in the presence of MFC compared with untreated cells (fig. S2A). Among these three candidates, septin 6 (SEPT6) reproducibly evoked the strongest response (fig. S2A). Rescreening of all septin isoforms present in the ORFeome collection confirmed binding of MFC to SEPT6 and revealed a weaker interaction with SEPT11, whereas none of the other septin isoforms tested interacted with MFC (Fig. 1F and fig. S2, B to D). A phylogenetic analysis of these septin isoforms showed that MFC interacts with the two most closely related SEPT6 family members, SEPT6 and SEPT11, and shows no detectable binding to the more distant SEPT2 and SEPT3 classes (Fig. 1F). SEPT6 is a guanosine 5'-triphosphate (GTP)-binding protein that assembles into filaments at the cell cortex together with SEPT2 and SEPT7 family members (31, 32). Septins regulate microtubule dynamics (33) and are present, together with hyperphosphorylated tau, in the neurofibrillary tangles of AD brains (34), pointing to a possible connection between tau and the septin cytoskeleton.

Next, we examined binding of REM127 to purified septin isoforms (fig. S3G) using flow-induced dispersion analysis (FIDA), a label- and immobilization-free technology that quantifies biomolecular interactions based on changes in size and diffusion (35). In these experiments, septin isoforms were maintained in high salt to prevent oligomerization (36). REM127 induced a dose-dependent increase in SEPT6 hydrodynamic radius, which, when fitted to a binding isotherm equation, revealed an apparent dissociation constant (K_d^{app}) of 1.5 nM (Fig. 1G and fig. S3A). Measuring K_d^{app} on the basis of binding-related (fluorescence) intensity change (BRIC) led to a comparable value (1.6 nM; Fig. 1H and fig. S3D). No compound-induced changes in hydrodynamic radius were detected for SEPT7 and SEPT2 (fig. S3, B and C), although binding isotherms associated with higher dissociation constants were observed by BRIC for both isoforms (Fig. 1, I and J, and fig. S3, E and F). These cell-free binding studies demonstrate direct and high-affinity binding of REM127 to SEPT6, with a possible impact on the target conformation. They also provide evidence for weaker binding of the compound to SEPT7 and SEPT2.

RNA interference (RNAi)-mediated silencing of SEPT6 attenuated the effects of REM127 on both toxicity and $[Ca^{2+}]_{cyto}$ (Fig. 1, K and L), confirming that SEPT6 participates in the ob-

served pharmacodynamic effects. Silencing was not complete (fig. S2E), and compound action through residual SEPT6 or other septin isoforms is to be anticipated. SEPT6 knockdown resulted in elevated toxicity and $[Ca^{2+}]_{cyto}$ at ineffective compound concentrations (Fig. 1, K and L), suggesting an inhibitory function of the target on $[Ca^{2+}]_{cyto}$.

ReS19-T suppresses SOCE induced by pathological tau

Septins have been identified as central regulators of SOCE (37, 38), a form of calcium influx activated by calcium depletion from the ER. To determine the impact of tau on SOCE at the single-cell level, we transfected neuroblastoma cells with tauP301L-T2A-mRuby, tau-T2A-mRuby, or mRuby DNA plasmids (fig. S4A) and imaged SOCE by calcium add-back after store depletion. tauP301L elicited a marked increase in basal $[Ca^{2+}]_{cyto}$ (before store depletion) and SOCE amplitude compared with WT tau or the mRuby control (Fig. 2A and fig. S4, B and C). Selecting cells with increasing amounts of tau expression (by gating mRuby intensity) revealed a corresponding increase in SOCE amplitude and $[Ca^{2+}]_{cyto}$ for both mutant and WT tau, although SOCE remained substantially larger in tauP301L-expressing cells (fig. S4B). As expected, SOCE responses in cells expressing mRuby alone were not influenced by the magnitude of mRuby expression (fig. S4B).

Exposing tauP301L-T2A-mRuby cells to REM127 normalized SOCE amplitude (Fig. 2, A and B) and basal $[Ca^{2+}]_{cyto}$ (Fig. 2, A and C). The compound lowered both calcium readouts in a dose-dependent manner (fig. S4, D and E). In marked contrast, REM127 left SOCE amplitude (Fig. 2B) and basal $[Ca^{2+}]_{cyto}$ (Fig. 2C) unchanged in mRuby cells. Selective targeting of tau-induced SOCE by REM127 was not observed with the store-operated calcium channel (SOCC) inhibitor Pyr6, which disrupted SOCE equally well in tauP301L-T2A-mRuby and mRuby cells (Fig. 2D and fig. S4F). Pyr6 also decreased basal $[Ca^{2+}]_{cyto}$ in tauP301L cells (Fig. 2E and fig. S4F), confirming that aberrant SOCC activation was responsible for the steady-state elevation of cytoplasmic calcium concentration in the pathological state. Short-term treatment with Pyr6, however, had no effect on basal $[Ca^{2+}]_{cyto}$ in control cells, further implying that SOCE is minimally active at steady state (in the absence of store depletion) unless tauP301L is expressed (Fig. 2E). Mutant tau can stimulate SOCE in store-replete cells because calcium stores (and their release) are unaffected by tauP301L expression (Fig. 2A and fig. S4C). Thus, the tauopathy-causing P301L mutation triggers a form of constitutive, store-independent but SOCC-mediated calcium entry that was selectively blocked by REM127.

We then investigated the function of SEPT6 in regulating SOCE. RNAi-mediated knockdown

of SEPT6 (fig. S2E) resulted in a marked increase in SOCE, similar to that caused by tauP301L (Fig. 2F), pointing to an inhibitory effect of the ReS19-T target on SOC channels and providing a potential mechanism for elevated steady-state $[Ca^{2+}]_{cyto}$ in SEPT6-silenced cells (Fig. 1L). Combined perturbations potentiated calcium entry in an additive manner (Fig. 2F).

To determine whether deranged SOCE and ensuing $[Ca^{2+}]_{cyto}$ overload would mediate toxicity in our tauP301L cell model, we manipulated SOC channel activity both pharmacologically and genetically. Two inhibitors of SOC channels, Pyr6 and BTP2, attenuated cell death (Fig. 2G) with median inhibitory concentrations near the potencies of the drugs for Orai channel inactivation (39). Similarly, small interfering RNA (siRNA)-mediated knockdown of stromal interaction molecule 1 (Stim1), an essential component of the SOCE machinery (37, 38), suppressed toxicity and occluded the compound effect (fig. S5, A to D). Finally, toxicity could also be alleviated (fig. S5E) by pharmacological stabilization of septin assembly with the small molecule forchlorfenuron (40), a perturbation reported to impair SOCE (37).

SOCCs are activated by the ER-resident Stim proteins at contact sites between the ER and the plasma membrane (PM). We thus investigated whether tau regulates the formation of ER-PM contact sites using the SPLICS_{short}-P2A^{ER-PM} probe, which specifically labels these membrane appositions (41). tauP301L augmented the interaction of the ER with the PM, and the increased contact area between these two membrane systems was lowered by REM127 (Fig. 2, H and I, and fig. S4G), which is in agreement with the inhibitory effect of the compound on tau-induced SOCE.

To assess the impact of REM127 on calcium effector pathways, we focused on the calcium/calmodulin-dependent phosphatase calcineurin (CaN), which activates the transcription factor NFAT (nuclear factor of activated T cells). Aberrant CaN and/or NFAT activity has been implicated in A β (42) and tau (43) pathology. tauP301L induces translocation of NFAT to the nucleus (in the absence of store depletion), and tau-mediated activation of this transcription factor was inhibited by REM127 or the CaN inhibitor cyclosporin A (Fig. 2, J and K, and fig. S4, H and I), indicating normalization of calcium-dependent signaling by REM127.

To examine SOCE in a more clinically relevant disease model, we turned to patient induced pluripotent stem cell (iPSC)-derived glutamate-releasing neurons (fig. S6, A and B). Neurons carrying the tauP301L mutation showed an increase in SOCE compared with their isogenic controls (Fig. 2, L and O), confirming enhanced SOC channel activity under conditions of tau pathology. REM127 decreased SOCE in tauP301L neurons in a

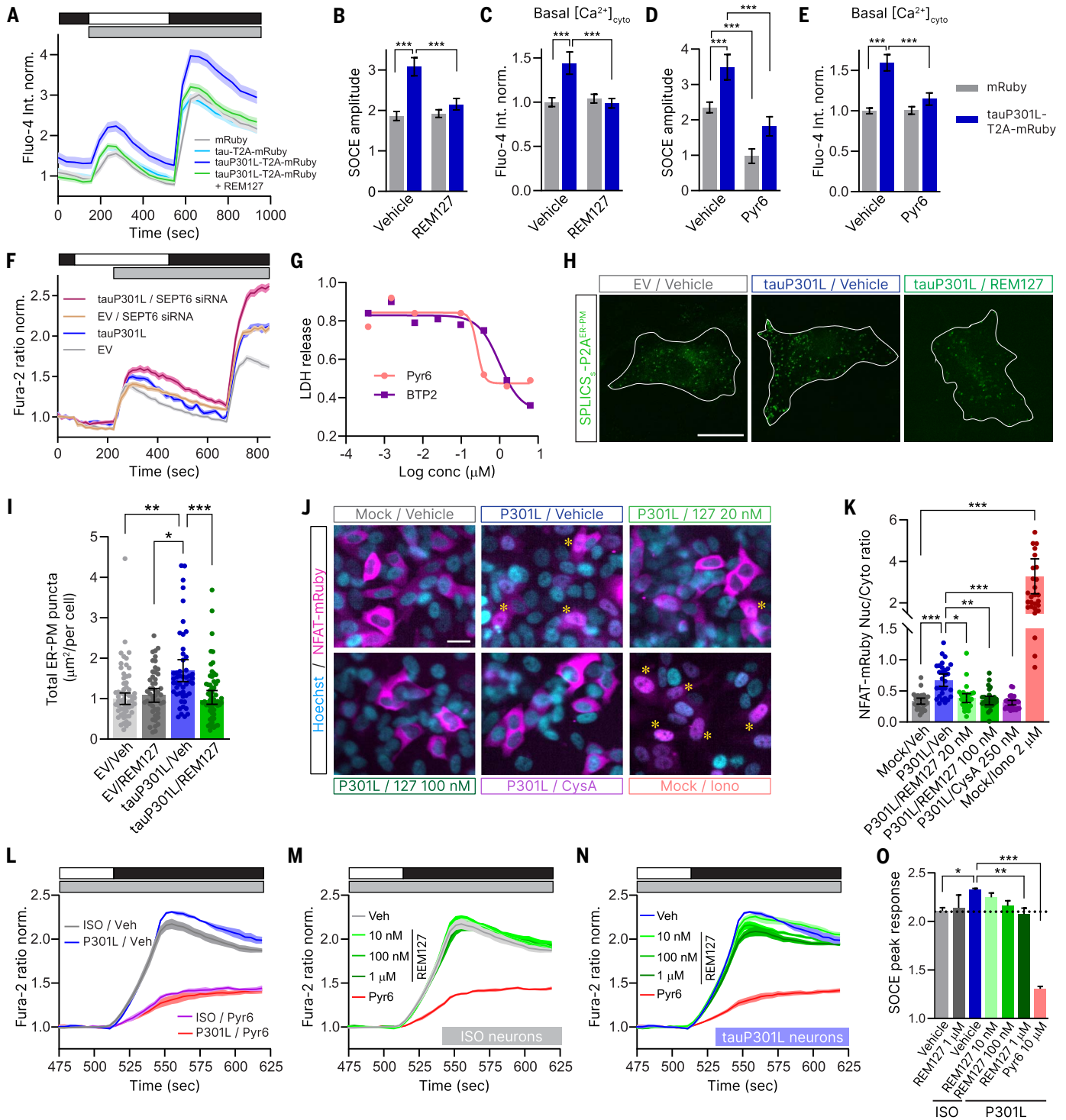


Fig. 2. ReS19-T specifically targets a tau-dependent pathological form of SOCE. (A to C) SOCE measured by calcium add-back in individual Fluo-4-loaded BE(2)-M17 cells transfected with the indicated constructs and exposed to vehicle [dimethyl sulfoxide (DMSO)] or REM127 (200 nM, 24 hours). (A) Fluo-4 traces normalized to the control mRuby/vehicle condition. (B and C) Average SOCE amplitude (B) and basal $[Ca^{2+}]_{cyto}$ (C) derived from time series shown in A. (D and E) Independent calcium add-back experiment showing average effect of Pyr6 (10 μ M, 1 hour) on SOCE amplitude and basal $[Ca^{2+}]_{cyto}$ in mRuby- or tauP301L-T2A-mRuby-expressing cells. In (A) to (E), >450 cells were analyzed for each condition. (F) SOCE measured in Fura-2-loaded BE(2)-M17 cells stably

expressing tauP301L or empty vector (EV) and transfected with scrambled or SEPT6-targeting siRNAs. Shown are average calcium traces (normalized to baseline) obtained from 24 replicate wells for each condition. (G) Lactate dehydrogenase (LDH) release in ATRA-treated tauP301L cells in the presence of increasing concentrations of the SOCC inhibitors Pyr6 and BTP2. (H and I) Imaging and quantification of ER-PM contact sites in control and tauP301L cells transfected with the ER-PM reporter SPPLCS_{short}-P2A^{ER-PM} and treated with vehicle or REM127 (100 nM, 24 hours). More than 45 cells were analyzed for each condition from three independent experiments. Scale bar, 10 μ m. (J and K) NFAT activity measured by nuclear translocation of mRuby-NFAT3 in mock or

tauP301L-transduced cells exposed to vehicle or REM127 (20 or 100 nM, 48 hours), cyclosporin A (250 nM, 24 hours), or ionomycin (2 μ M, 1 hour). (J) Confocal images showing mRuby-NFAT localization in response to indicated treatments. Scale bar, 20 μ m. Yellow asterisks point to cells with clear nuclear localization of mRuby-NFAT. (K) mRuby-NFAT nucleus-to-cytoplasm intensity ratio measured for indicated treatments. $N = 30$ cells for each condition. (L to O) SOCE measured in Fura-2-loaded patient-derived glutamatergic neurons (tauP301L) or isogenic controls cultured for 90 DIV. $N = 3$ replicate wells for each condition. (O)

concentration-dependent manner (Fig. 2, N and O) but had no detectable effect in control neurons (Fig. 2, M and O). Maximal inhibition by REM127 reduced the SOCE response to that seen in isogenic neurons, whereas blockade of SOC channels with Pyr6 resulted in a pronounced inhibition of calcium entry in both control and tauP301L neurons (Fig. 2, L to O).

ReS19-T influences the dynamics of septin filament assembly

Septins have recently been shown to organize ER-PM contact sites (37, 38), pinpointing a possible mechanism of action for REM127. To test the influence of REM127 on the septin cytoskeleton, we first explored the space of potential binding pockets in the palindromic SEPT2/6/7 hexamer (Fig. 3A), which forms the minimal core unit for filament polymerization. To this end, we used Ligand Gaussian Accelerated Molecular Dynamics (LiGaMD), a computational method particularly suited to sampling the entire conformational space of a ligand around a protein of interest (44). A recent cryo-electron microscopy structure of the human SEPT2/6/7 hexamer (45) refined with AlphaFold 2.0 (46) was used for these simulations. Because septins are guanosine nucleotide-binding proteins, we considered eight simulation systems, each differing in the number of guanosine diphosphate (GDP) or GTP molecules (fig. S7A). REM127-binding hotspots were identified at the SEPT6/7 interface in seven systems (fig. S7A). In the nucleotide-free system, REM127 binds near the SEPT7 GDP-binding pocket with the weakest affinity (fig. S7A). In septin oligomers, subunits present alternating NC (N- and C-termini) and G (GTP-binding) interfaces (Fig. 3A). The SEPT6/7 interface is of the NC type, consistent with minimal influence of GDP/GTP occupancy on REM127 binding.

Figure 3A shows the simulation outcome with the most energetically favorable REM127 binding pose. REM127 lies deep in the SEPT6/7 NC interface (Fig. 3, A and B) and makes direct contact with several amino acids located on both SEPT6 and SEPT7 (Fig. 3, B and C). The compound also makes hydrogen bonds with the backbone oxygen of asparagine 1175 on SEPT6, and possibly with glutamate 890 and/or lysine 1138 on SEPT7, depending on the protonation state of its thiadiazol ring (Fig. 3B). Extensive contact of the compound

along the SEPT6/7 interface suggests a possible impact on SEPT6/7 dimer conformation and stability. To address this computationally, we measured binding free energy between SEPT6 and SEPT7 in the presence or absence of REM127 and in response to a wide range of pulling forces until complete disruption of the dimer. These umbrella sampling calculations revealed an end-point difference of 30 kcal/mol between ligand-bound and ligand-free states (Fig. 3D), indicating that disruption of the ligand-bound system is energetically more costly and suggesting stabilization of the SEPT6/7 dimer by REM127.

Because REM127 binds to purified SEPT6 alone (Fig. 1, G and H), we used LiGaMD to simulate binding of the compound to the SEPT6 homodimer, which is the preferred state of purified septins in nonpolymerizing conditions (47). Modeling of the SEPT6 homodimer by AlphaFold 2.0 predicted an NC interface (fig. S7B), and LiGaMD identified a REM127-binding hotspot in the cavity created by the NC interface in the SEPT6 homodimer (fig. S7C), like the one observed at the SEPT6/7 interface in the septin hexamer.

Anticipating efficacy studies in mouse models, we investigated binding of REM127 to the mouse SEPT6/7 interface. The amino acids predicted by LiGaMD to contact REM127 at the human SEPT6/7 interface (Fig. 3C and fig. S8A) are fully conserved in the mouse orthologs (fig. S8, A and B). We modeled the mouse SEPT6/7 heterodimer using AlphaFold 2.0 (there is no structure of mouse septins available) and simulated interaction of the compound using molecular dynamics. As for the human system, REM127 stably associated with the mouse SEPT6/7 interface throughout the course of these simulations (fig. S8, C and D). The compound, however, adopts distinct binding poses (fig. S8C) suggesting a more flexible binding mode compared with the one observed at the human SEPT6/7 interface. A close examination of the mouse and human AlphaFold structures reveals subtle species-specific differences near the interface that may influence ligand binding (fig. S8, E and F). Despite slight differences in binding conformation, REM127 lines up along the mouse SEPT6/7 interface and makes contact with multiple amino acids located on both SEPT6 and SEPT7 (fig. S8G), consistent with stabilization of the mouse heterodimer.

Quantification of peak SOCE responses in control and tauP301L neurons treated with increasing concentrations of REM127 for 24 hours or Pyr6 (10 μ M, 1 hour). In (A), (F), (L), (M) and (N), bars on top of time series indicate the presence (black) or absence (white) of extracellular calcium, and thapsigargin treatment (gray). Shaded error bars represent 95% CI. * $P < 0.05$, ** $P < 0.01$, *** $P < 0.001$, one-way ANOVA with multiple pairwise comparisons of means (Tukey's test) in (B) to (E) and (O) and Kruskal-Wallis with Dunn's multiple-comparisons test in (I) and (K). See also corresponding figs. S4 to S6.

To experimentally investigate the effect of REM127 on septin polymerization, we mixed purified (human) SEPT2, SEPT6, and SEPT7 in conditions that favor filament assembly and monitored polymerization at different time points by dynamic light scattering (DLS) and transmission electron microscopy (TEM). A clear shift toward higher particle sizes (>500 nm) was detected by DLS 90 min after component mixing (Fig. 3E). Addition of GTP γ S, a non-hydrolyzable form of GTP that can promote septin assembly (48), accelerated the formation of larger particles with an effect noticeable immediately after component mixing (Fig. 3E). Likewise, REM127 shifted the distribution of particles toward larger sizes, with kinetics comparable to GTP γ S (Fig. 3E). Consistent with these DLS measurements, TEM images showed that both GTP γ S and REM127 induced the formation of polymerized structures shortly after component mixing (Fig. 3F). No or few such structures were detected in the vehicle condition at early time points (Fig. 3F). At 6 hours after mixing, highly ordered filaments appeared in the REM127-treated samples, the number of which substantially increased in the following 18 hours (Fig. 3F).

Although micrometer-long polymers were also observed in vehicle and GTP γ S conditions 24 hours after mixing, their structure differed substantially from the linear pattern of polymerization generated by REM127, suggesting distinct mechanisms of action. In support of this view, REM127 is predicted to bind and stabilize the SEPT6/7 NC interface, whereas GTP (and GTP γ S) interacts with G interfaces in the polymer.

To assess whether septin filaments are influenced by tau and REM127 within cells, we monitored the endogenous state of septin polymerization. Because SEPT6 antibodies failed to label distinct cytoskeletal structures, we used instead a SEPT2 antibody that stains filaments that colocalize with exogenous GFP-SEPT6 (fig. S9A). In control conditions, the antibody decorates filaments at the cell cortex, but these undergo major remodeling to circular, doughnut-like structures in response to tauP301L expression (Fig. 4, A, B, and D). Treatment with REM127 restored the fibrillar organization of SEPT2 near the PM (Fig. 4, C and D). A repeat of this experiment in a mouse neuroblastoma cell line showed similar rescue of cortical septin localization by REM127 in

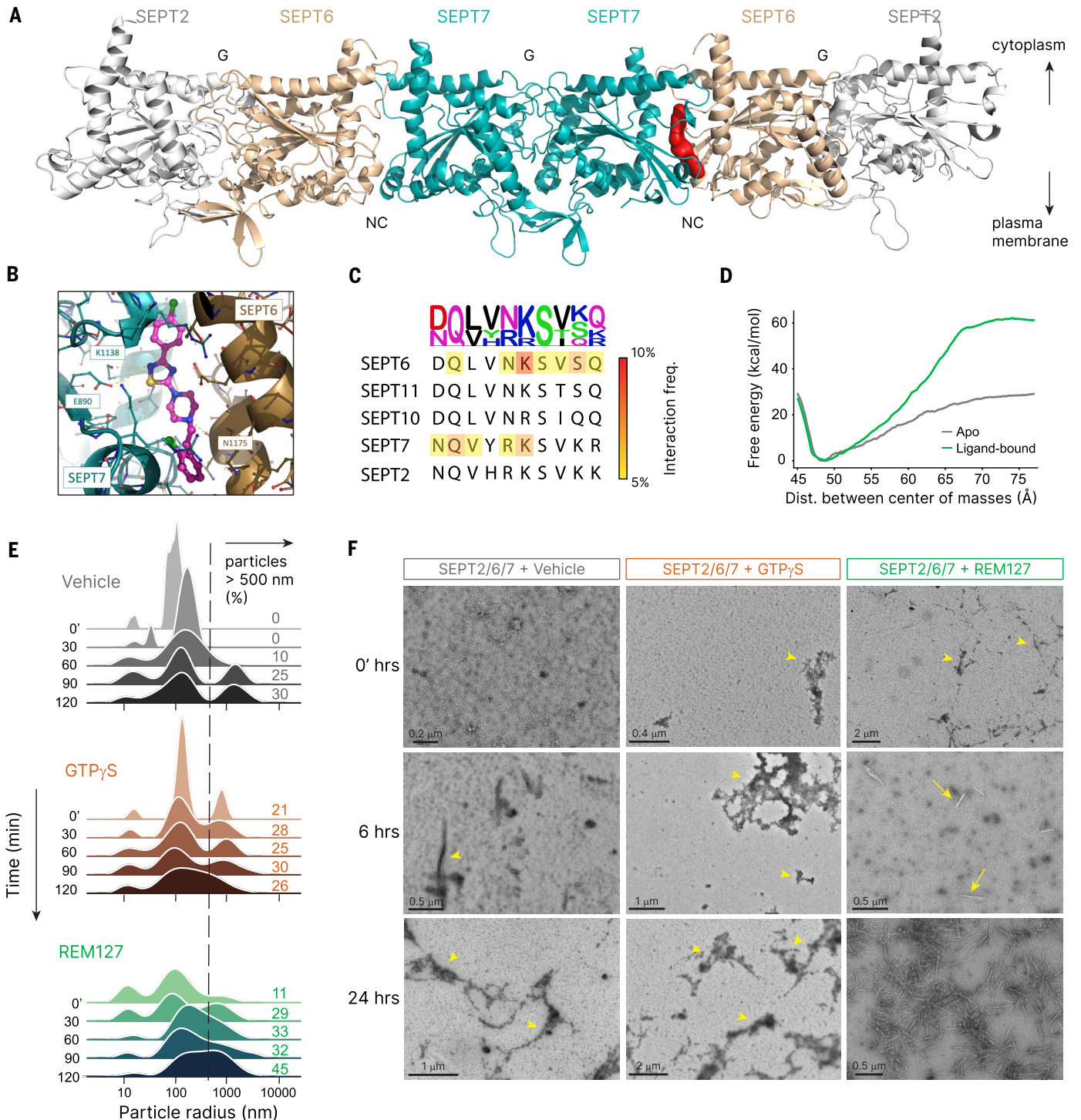


Fig. 3. ReS19-T influences septin filament assembly in cell-free conditions.

(A to D) LiGaMD simulations of REM127 interaction with the SEPT2/6/7 hexamer. (A) LiGaMD identifies a high-affinity binding pocket at the NC interface between SEPT6 and SEPT7. REM127 is shown in red. (B) Blow up of the SEPT6/7 interface with amino acids predicted to interact with REM127. Hydrogen bonds formed by the compound with surrounding amino acids are shown in yellow. Amino acids are labeled according to their position in the SEPT2/6/7 hexamer. (C) Alignment showing the main cluster of amino acids in SEPT6 and SEPT7 interacting with REM127. Heatmap indicates the frequency of interactions. Amino acid conservation and type are shown at the top using the sequence logo. (D) Umbrella sampling calculations of the SEPT6/7

heterodimer showing binding free energy with and without bound ligand. (E and F) Cell-free assembly of SEPT2/6/7 filaments. (E) DLS measurements performed at different time points after mixing of purified SEPT2, SEPT6, and SEPT7 (500 nM final protein concentration) in the presence of vehicle (DMSO), GTP γ S (100 μ M), or REM127 (1 μ M). 0' indicates the first measurement immediately after component mixing. Distribution of particle size (y axis) is normalized across treatment and time points. (F) TEM images of SEPT2/6/7 polymerization performed in conditions identical to (E) and captured at three time points after component mixing. Arrowheads point to typical polymerized structures. Arrows point to highly ordered filaments only observed after REM127 treatment. See also corresponding figs. S7 and S8.

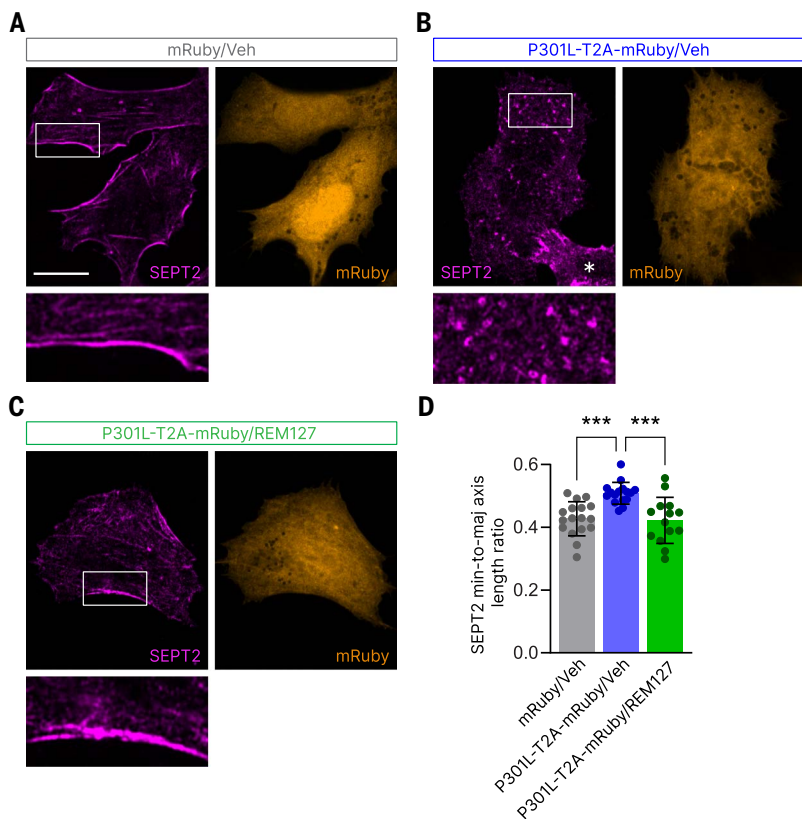


Fig. 4. ReS19-T rescues septin filament assembly in cells expressing pathogenic tau. (A to C) SEPT2 immunostaining in BE(2)-M17 cells transfected with mRuby or tauP301L-T2A-mRuby and treated for 24 hours with REM127 (100 nM) or vehicle. The asterisk indicates a nontransfected cell. Scale bar, 10 μ m. (D) Quantification of SEPT2 circular versus filamentous structures by measuring the average minor to major axis length ratio for all SEPT2 objects segmented in individual cells ($N > 13$ for each group). *** $P < 0.001$, one-way ANOVA with multiple pairwise comparisons of means (Tukey's test). See also corresponding fig. S9.

tauP301L-expressing cells (fig. S9, B to E), confirming target engagement of mouse septins by the compound.

Collectively, these experiments support the following sequence of events: tauP301L destabilizes the cortical septin cytoskeleton, resulting in increased ER-PM contact area and constitutive activation of SOCCs. By restoring filament assembly at the PM, REM127 limits ER-PM contacts and keeps the activity of SOCCs in check.

Modulation of septins by ReS19-T restores network function in patient-derived iPSC neurons and AD mouse models

$[Ca^{2+}]_{cyto}$ overload has been associated with hyperexcitability and synaptic dysfunction in AD. To assess whether patient-derived excitatory neurons are hyperexcitable, we compared the spontaneous firing frequency of glutamate-releasing tauP301L neurons and their isogenic controls by longitudinal measurements of calcium spike activity over the course of 20 days. The mean burst rate was markedly increased in tauP301L neurons at all time points investigated, and this hyper-

excitability phenotype was progressively and fully rescued by REM127 (Fig. 5, A and B).

The effect of REM127 on synaptic plasticity was next examined in transgenic mice expressing either human tauP301S, a mutation causing FTD (49), or the APP London mutant carrying the familial AD mutation V717I (APP-Ln). Both models of neurodegeneration showed severe deficits in long-term potentiation (LTP) in the CA1 region of the hippocampus (Fig. 5, C and D), a form of activity- and calcium-dependent increase in synaptic efficacy associated with learning and memory. Oral administration of REM127 restored LTP in both tauP301S and APP-Ln mice (Fig. 5, C and D). A 7-day treatment with the compound was sufficient to rescue LTP in APP-Ln mice (Fig. 5D). Similar effects on LTP, both in terms of magnitude and kinetics, were observed with REM123 (fig. S10), a close analog of REM127 (fig. S1B). Combining pharmacokinetic studies with LTP measurements enabled us to establish the exposure-response relationship for REM127 (Fig. 5, E and F, and table S1). This analysis revealed a median effective dose of 6 mg/kg/day (table S1), corresponding to an

average unbound concentration of REM127 in the brain of 12 nM, an EC_{50} in agreement with the potency of the compound measured in vitro (Fig. 1A). REM127 had no effect on LTP in WT animals (Fig. 5G), reflecting an activity restricted to the disease state.

Rapid modulation of neuronal excitability and synaptic plasticity by REM127 prompted us to test the influence of the compound on brain oscillatory activity. Electroencephalography (EEG) recordings from individuals with AD indicate increased power in low-frequency theta rhythms, which correlates with poor cognitive performance and is increasingly recognized as a potential biomarker (50, 51). Likewise, a higher magnitude of low-frequency bands was observed here in awake APP-Ln mice (Fig. 5H). Administration of REM127 for 2 weeks normalized power spectral density (Fig. 5H), demonstrating the broad impact of the compound on network function.

We then tested the ability of ReS19-T to rescue spatial memory deficits in APP-Ln mice using the Morris water maze behavioral paradigm. Mice carrying the APP mutation needed more trials to learn how to navigate to a hidden escape platform, but by the end of the fourth training day, their performance was undistinguishable from that of nontransgenic animals (Fig. 5I). However, when subsequently tested for memory recall (in the absence of the escape platform), transgenic animals displayed a marked deficit in performance (Fig. 5J). Impairment in memory retention, with no apparent learning deficits at the end of the training period, has previously been reported in AD mouse models (52, 53). This dissociation in performance was used in a recent mouse behavioral study to suggest that the familial V717F mutation in APP interferes with memory retrieval rather than memory encoding (52). Treatment of APP-Ln mice with REM123 had no significant influence on performance during the training period (Fig. 5I) but fully rescued spatial memory in the recall test (Fig. 5J), suggesting restoration of neural circuits underlying retrieval of spatial memories.

ReS19-T mitigates the development of AD pathology

In addition to mediating degeneration of neurons, aberrant calcium signaling is thought to promote the development of AD pathology (11–13). Therefore, we hypothesized that restraining calcium influx in diseased neurons by ReS19-T should mitigate pathology in AD mouse models. Treatment of bigenic APP-Ln: PS1(A246E) with REM127 for 3 months resulted in a 55 to 60% reduction of A β plaque buildup in the neocortex (Fig. 6, A and B, and fig. S11, A and B) and subiculum (Fig. 6, A and C), a structure that connects the entorhinal cortex to the hippocampus. Both brain regions are prominently affected in AD. In the same mutant

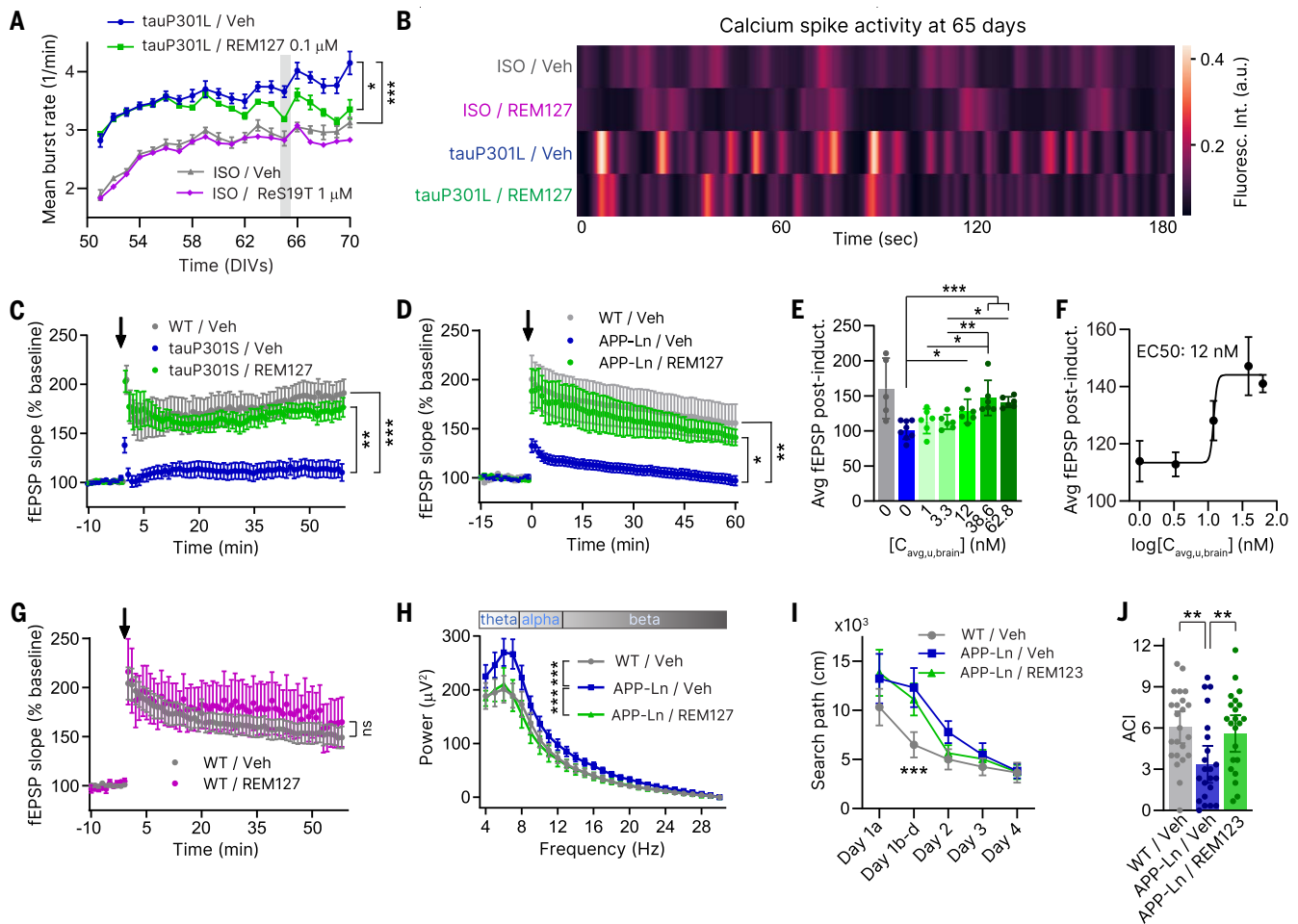


Fig. 5. Rapid restoration of synaptic, network, and cognitive functions by ReS19-T in AD preclinical models. (A) Spontaneous calcium spike activity in patient-derived tauP301L neurons and their isogenic controls exposed to vehicle or REM127 at the indicated concentrations. Mean frequency of calcium bursts was measured for 3 min over a period of 20 days from DIV 50 to 70 (three replicate wells for each condition). (B) Calcium spike activity measured 15 days after the first recording and corresponding to time point highlighted in gray in (A). (C) CA1 LTP in WT and tauP301S mice (3.5 months of age, $N = 8$ for each group) administered with vehicle or REM127 (20 mg/kg/day) for 2 months. Arrow indicates tetanus LTP inducing stimulus. (D) CA1 LTP in WT/Veh ($N = 5$), APP-Ln/Veh ($N = 8$), and APP-Ln/REM127 ($N = 6$) mice (7 months of age) administered with vehicle or REM127 (20 mg/kg/day) for 7 days. (E and F) Exposure-dependent rescue of LTP in APP-Ln mice. $C_{\text{avg,u,brain}}$: average free brain concentration of REM127 calculated from in vivo pharmacokinetic profile of the compound (table S1). Statistics were only performed within the

APP-Ln group to identify exposure-dependent effects on LTP. (G) LTP in WT animals (3.5 months of age) administered with vehicle ($N = 11$) or REM127 ($N = 6$) at 20 mg/kg/day for 7 days. (H) Power analysis of EEG recordings (parietal lobe) in awake WT/Veh ($N = 6$), APP-Ln/Veh ($N = 8$), and APP-Ln/REM127 ($N = 4$) mice, 8 months of age, administered with vehicle or REM127 (20 mg/kg/day) for 14 days. (I and J) Morris water maze results. Shown are spatial learning (I) and memory recall (annulus crossing index) (J) in WT/Veh ($N = 23$), APP-Ln/Veh ($N = 23$), and APP-Ln/REM123 ($N = 23$) mice 8 months of age that were administered with vehicle or REM123 (20 mg/kg/day) for 11 weeks. Error bars indicate SEM, except for (E), where they correspond to SD. $*P < 0.05$, $**P < 0.01$, and $***P < 0.001$, one-way ANOVA with multiple pairwise comparisons of means (Tukey's test) in (A), (C) to (E), and (J); unpaired t test in (G); two-way ANOVA with repeated measures (RM) with genotype or treatment as the between-subject factor and frequency as the within subject factor in (H); and two-way ANOVA with RM and Sidak pairwise multiple-comparisons test in (I). See also corresponding fig. S10.

mice, the compound also reduced microglial inflammation associated with AD pathology (Fig. 6D). Additionally, REM127 decreased dense-core amyloid plaques (Fig. 6, E and F) and $A\beta_{42}$ production (Fig. 6G) in the prefrontal cortex of APP-SAA mice, a recently developed knock-in model of AD (54). Co-staining of fibrillar $A\beta$ with the AT8 epitope revealed the presence of phosphorylated tau aggregates in the center of plaques, a clear sign of tau pathology. Treatment with REM127 markedly reduced AT8 immunoreactivity in APP-SAA mice

(Fig. 6, H and I). However, REM127 had no detectable influence on diffuse amyloid plaques in these knock-in mice (fig. S11C), even though the compound affects the dense core of these plaques (Fig. 6, E and F). In the more aggressive APP-Ln:PS1(A246E) model, in which the dense core accounts for a larger portion of total plaque area (fig. S11D), REM127 lowered both total and dense plaque load (Fig. 6, A to C, and fig. S11, A and B). These subtle differences in compound activity likely reflect model-specific abundance, processing, and aggregation

of $A\beta$ peptides, but it is also possible that REM127 preferentially targets the core of $A\beta$ plaques, where tau pathology and presumably $[Ca^{2+}]_{\text{cyto}}$ are high. Finally, we examined the impact of ReS19-T in tauP301S mice, a model that exhibits severe tau pathology without amyloid deposition. Treatment of these mice with the REM127 regioisomer REM123 lowered the concentration of tau in the cerebrospinal fluid (Fig. 6J), a clinical AD biomarker, which is consistent with calcium-dependent tau secretion (14). REM123 also decreased tau phosphorylation in

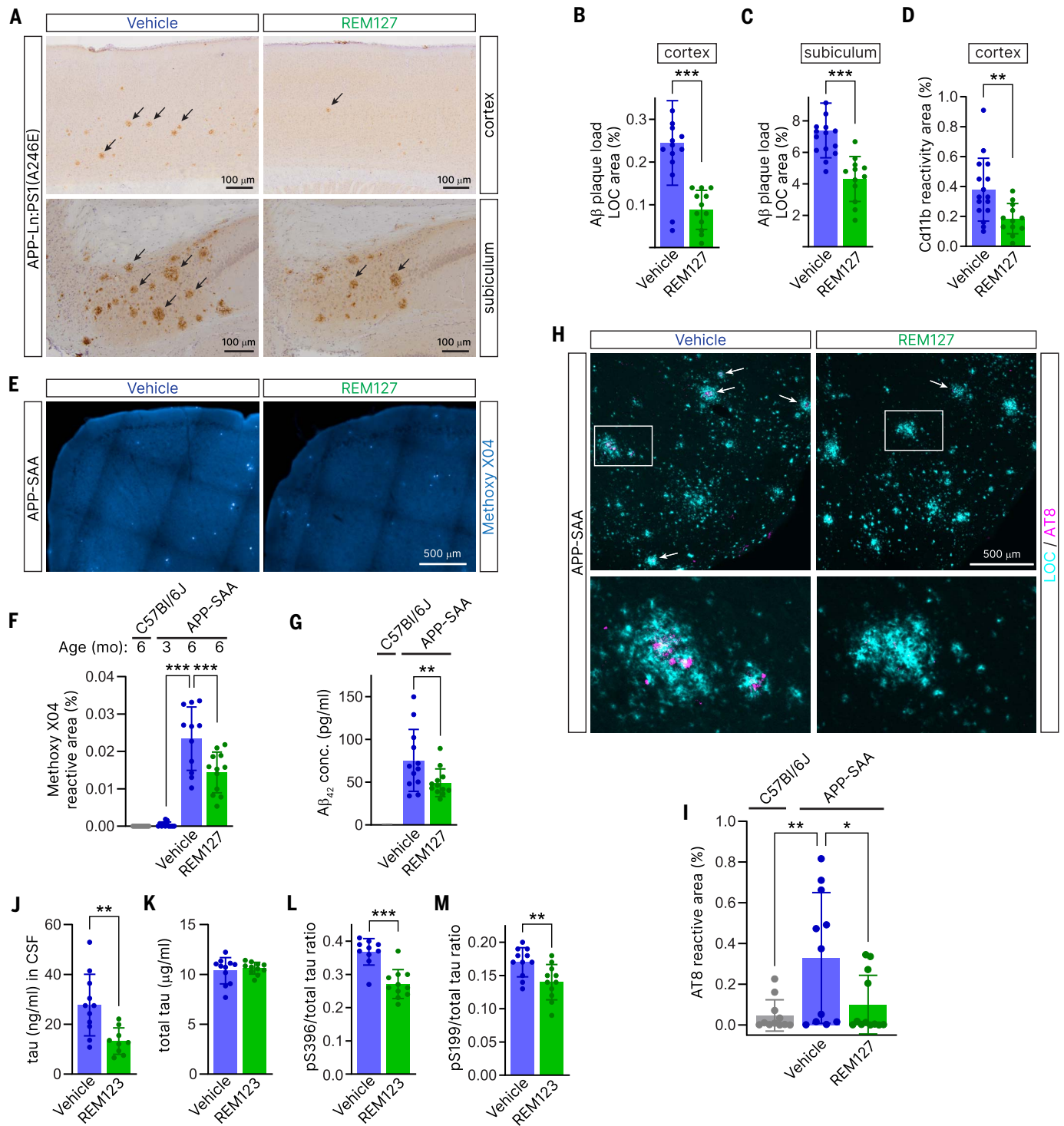


Fig. 6. ReS19-T attenuates AD pathology. (A to D) APP-Ln:PS1(A246E) mice (7 months old) after 3 months of vehicle ($N = 16$) or REM127 ($N = 12$) oral dosing at 20 mg/kg/day. (A to C) Aβ plaques stained with an anti-amyloid fibrils (LOC) antibody in cortex [(A) and (B)] and subiculum [(A) and (C)]. (D) CD11b immunoreactivity in cortex. (E to G) Dense core staining of Aβ plaques with Methoxy X04 in prefrontal cortex [(E) and (F)] and measurements of Aβ₄₂ concentration in the soluble fraction of the cortex (G) of APP-SAA mice and C57Bl/6J controls orally dosed with vehicle or REM127 (25 mg/kg/day) for 3 months. $N = 11$ to 12 for each group. (H and I) Co-staining of Aβ fibrils (LOC)

and phospho-tau (p-Ser202 and p-Thr205) using the AT8 antibody in same animal cohorts described in (E) to (G). (J to M) Five-month-old tauP301S mice treated for 3 months with vehicle or REM123 at 20 mg/kg/day. (J) Tau concentration in CSF measured by ELISA ($N > 9$ for each group). Pan-tau (K), pS396-tau (L), and pS199-tau (M) were measured by ELISA in cortical extracts ($N = 11$ for each group). Error bars indicate SD. * $P < 0.05$, ** $P < 0.01$, and *** $P < 0.001$, unpaired t test, in (B) to (D) and (J) to (M) and one-way ANOVA with multiple pairwise comparisons of means (Tukey's test) in (F) to (I). See also corresponding fig. S11.

cortical brain extracts of these mice (Fig. 6, K to M). Thus, ReS19-T compounds attenuate the main pathological features of AD.

Discussion

Here, we show broad therapeutic benefits of a class of small molecules (ReS19-T) that target calcium dysregulation induced by pathological tau, providing further support for a key role of aberrant $[Ca^{2+}]_{cyto}$ in driving neurodegeneration. Restoration of synaptic plasticity (LTP) and normal brain network activity (EEG) in APP-Ln mice was observed after only 7 to 14 days of treatment, indicating rapid relief of A β -driven toxicity in the underlying neural circuits. This effect is consistent with fast-acting decrease in $[Ca^{2+}]_{cyto}$ by ReS19-T and down-regulation of CaN activity, a calcium-activated phosphatase centrally implicated in synaptic depression, memory erasure, and A β -induced synapse disruption (55, 56). ReS19-T not only protects against acute A β /tau-induced neurotoxicity but also mitigates the development of A β and tau pathology. This implies the existence of a self-amplifying loop between elevated $[Ca^{2+}]_{cyto}$ and A β /tau pathology (18). By lowering $[Ca^{2+}]_{cyto}$, ReS19-T disrupts this harmful cycle rapidly and efficiently. This model of pathogenesis and pharmacological intervention can be extended, in principle, to risk factors associated with sporadic AD (e.g., aging and mitochondrial dysfunction) and to other tauopathies that manifest with early disturbances in $[Ca^{2+}]_{cyto}$ (18).

Our findings suggest that aberrant calcium entry is an integral component of tau pathology, in agreement with a recent study identifying genes associated with calcium homeostasis as being primary modifiers of tau-induced toxicity (57). The effect of ReS19-T on pathological SOCC activation was investigated in the context of a tau mutation (P301L) that causes FTD. Because this mutation induces tau hyperphosphorylation, and aggregation (hallmarks of all tauopathies, including AD), we propose that similar disease and compound mechanisms are at play in AD.

Accumulating evidence points to reciprocal influence of A β and tau in AD (58). Although the impact of A β on the initiation of tau pathology is undisputed (tau is hyperphosphorylated in many APP models, (including the ones used here), tau has also been shown to enhance and, in some cases, mediate aspects of A β pathology (59). On the basis of these observations and on the stimulatory effect of calcium on A β peptide production (12), we surmise that the inhibitory effect of ReS19-T on A β pathology (A β plaques and A β_{42} amounts) is due, at least in part, to its normalizing activity on tau-induced calcium dysregulation.

We provide evidence that tau-induced SOCC activation and compound activity are both linked to the septin cytoskeleton. In nonpath-

ological conditions, septin filaments at the cell cortex restrain SOCE and inhibit constitutive (store-independent) activation of SOCCs. In support of this “gatekeeper” function, silencing of SEPT6 (this study) or SEPT7 (38, 60, 61) results in unimpeded SOCE activity. Knockdown of SEPT2 family members (SEPT2, SEPT4, and SEPT5), by contrast, has been reported to suppress SOCE (37), highlighting complex modulatory roles of septin isoforms in SOCC regulation. In conditions of tau pathology, filament organization of septins at the PM is altered, and this is associated with an increase in ER-PM contact sites, thus providing a mechanism for uncontrolled activation of SOCCs. By restoring septin organization at the cell cortex in the disease state, ReS19-T rehabilitates an important element of physiological SOCC regulation, which prevents spurious activation of the channel in store-replete conditions. Together, these findings reveal a mechanism of action restricted to the pathological state, where ReS19-T operates on a form of deviant SOCC activation found only in conditions of tau pathology.

Perturbed expression and mislocalization of different septin isoforms have previously been associated with neurodegeneration. SEPT1, SEPT2, and SEPT4 are found in neurofibrillary tangles and dystrophic neurites in AD (34), whereas SEPT4 colocalizes with α -synuclein in Parkinson’s disease Lewy bodies (62), and SEPT11, a close homolog of SEPT6, is enriched in insoluble fractions in frontotemporal lobar degeneration (63). We show here that pharmacological modulation of septin assembly results in broad neuroprotective effects in cell, mouse, and patient-derived iPSC models of neurodegeneration, suggesting a central role of septin filaments in AD pathogenesis.

In summary, this work highlights the therapeutic potential of calcium-lowering interventions in AD and FTD and holds promise for a small-molecule-based alternative to A β -targeting therapies. The anticipated therapeutic benefits of ReS19-T in individuals with AD are currently being evaluated in clinical trials.

Methods summary

A full description of the methods can be found in the supplementary materials. This includes descriptions of all ReS19-T compounds, DNA constructs, and mouse models used in this study; target identification and molecular dynamics simulations; cell-based imaging protocols; electrophysiology and immunocytochemistry on brain slices; in vivo EEG recordings; and statistical tests.

REFERENCES AND NOTES

1. P. Scheltens *et al.*, Alzheimer’s disease. *Lancet* **397**, 1577–1590 (2021). doi: [10.1016/S0140-6736\(20\)32205-4](https://doi.org/10.1016/S0140-6736(20)32205-4); pmid: [33667416](https://pubmed.ncbi.nlm.nih.gov/33667416/)
2. M. A. Leissring *et al.*, Capacitative calcium entry deficits and elevated luminal calcium content in mutant presenilin-1

- knockin mice. *J. Cell Biol.* **149**, 793–798 (2000). doi: [10.1083/jcb.149.4.793](https://doi.org/10.1083/jcb.149.4.793); pmid: [10811821](https://pubmed.ncbi.nlm.nih.gov/10811821/)
3. R. Etcheberrigaray *et al.*, Calcium responses in fibroblasts from asymptomatic members of Alzheimer’s disease families. *Neurobiol. Dis.* **5**, 37–45 (1998). doi: [10.1006/mbdi.1998.0176](https://doi.org/10.1006/mbdi.1998.0176); pmid: [9702786](https://pubmed.ncbi.nlm.nih.gov/9702786/)
4. Q. Guo *et al.*, Increased vulnerability of hippocampal neurons to excitotoxic necrosis in presenilin-1 mutant knock-in mice. *Nat. Med.* **5**, 101–106 (1999). doi: [10.1038/4789](https://doi.org/10.1038/4789); pmid: [9883847](https://pubmed.ncbi.nlm.nih.gov/9883847/)
5. J. Larson, G. Lynch, D. Games, P. Seubert, Alterations in synaptic transmission and long-term potentiation in hippocampal slices from young and aged PDAPP mice. *Brain Res.* **840**, 23–35 (1999). doi: [10.1016/S0006-8993\(99\)01698-4](https://doi.org/10.1016/S0006-8993(99)01698-4); pmid: [10517949](https://pubmed.ncbi.nlm.nih.gov/10517949/)
6. S. Chakroborty *et al.*, Early presynaptic and postsynaptic calcium signaling abnormalities mask underlying synaptic depression in presymptomatic Alzheimer’s disease mice. *J. Neurosci.* **32**, 8341–8353 (2012). doi: [10.1523/JNEUROSCI.0936-12.2012](https://doi.org/10.1523/JNEUROSCI.0936-12.2012); pmid: [22699914](https://pubmed.ncbi.nlm.nih.gov/22699914/)
7. S. Forner, D. Baglietto-Vargas, A. C. Martini, L. Trujillo-Estrada, F. M. LaFerla, Synaptic impairment in Alzheimer’s disease: A dysregulated symphony. *Trends Neurosci.* **40**, 347–357 (2017). doi: [10.1016/j.tins.2017.04.002](https://doi.org/10.1016/j.tins.2017.04.002); pmid: [28494972](https://pubmed.ncbi.nlm.nih.gov/28494972/)
8. D. J. Selkoe, Alzheimer’s disease is a synaptic failure. *Science* **298**, 789–791 (2002). doi: [10.1126/science.1074069](https://doi.org/10.1126/science.1074069); pmid: [12399581](https://pubmed.ncbi.nlm.nih.gov/12399581/)
9. M. J. Berridge, Calcium regulation of neural rhythms, memory and Alzheimer’s disease. *J. Physiol.* **592**, 281–293 (2014). doi: [10.1113/jphysiol.2013.257527](https://doi.org/10.1113/jphysiol.2013.257527); pmid: [23753528](https://pubmed.ncbi.nlm.nih.gov/23753528/)
10. E. Popugaeva, D. Chernyuk, I. Bezprozvanny, Reversal of calcium dysregulation as potential approach for treating Alzheimer’s disease. *Curr. Alzheimer Res.* **17**, 344–354 (2020). doi: [10.2174/1567205017666200528162046](https://doi.org/10.2174/1567205017666200528162046); pmid: [32469698](https://pubmed.ncbi.nlm.nih.gov/32469698/)
11. H. W. Querfurth, J. Jiang, J. D. Geiger, D. J. Selkoe, Caffeine stimulates amyloid beta-peptide release from beta-amyloid precursor protein-transfected HEK293 cells. *J. Neurochem.* **69**, 1580–1591 (1997). doi: [10.1046/j.1471-4159.1997.69041580.x](https://doi.org/10.1046/j.1471-4159.1997.69041580.x); pmid: [9326287](https://pubmed.ncbi.nlm.nih.gov/9326287/)
12. H. W. Querfurth, D. J. Selkoe, Calcium ionophore increases amyloid beta peptide production by cultured cells. *Biochemistry* **33**, 4550–4561 (1994). doi: [10.1021/bi00181a016](https://doi.org/10.1021/bi00181a016); pmid: [8161510](https://pubmed.ncbi.nlm.nih.gov/8161510/)
13. N. Pierrot *et al.*, Calcium-mediated transient phosphorylation of tau and amyloid precursor protein followed by intraneuronal amyloid-beta accumulation. *J. Biol. Chem.* **281**, 39907–39914 (2006). doi: [10.1074/jbc.M606015200](https://doi.org/10.1074/jbc.M606015200); pmid: [17085446](https://pubmed.ncbi.nlm.nih.gov/17085446/)
14. A. M. Pooler, E. C. Phillips, D. H. W. Lau, W. Noble, D. P. Hanger, Physiological release of endogenous tau is stimulated by neuronal activity. *EMBO Rep.* **14**, 389–394 (2013). doi: [10.1038/embor.2013.15](https://doi.org/10.1038/embor.2013.15); pmid: [23412472](https://pubmed.ncbi.nlm.nih.gov/23412472/)
15. H. Hsieh *et al.*, AMPAR removal underlies Abeta-induced synaptic depression and dendritic spine loss. *Neuron* **52**, 831–843 (2006). doi: [10.1016/j.neuron.2006.10.035](https://doi.org/10.1016/j.neuron.2006.10.035); pmid: [17455504](https://pubmed.ncbi.nlm.nih.gov/17455504/)
16. S. H. Zaman *et al.*, Enhanced synaptic potentiation in transgenic mice expressing presenilin 1 familial Alzheimer’s disease mutation is normalized with a benzodiazepine. *Neurobiol. Dis.* **7**, 54–63 (2000). doi: [10.1006/mbdi.1999.0271](https://doi.org/10.1006/mbdi.1999.0271); pmid: [10671322](https://pubmed.ncbi.nlm.nih.gov/10671322/)
17. S. Chakroborty, I. Goussakov, M. B. Miller, G. E. Stutzmann, Deviant ryanodine receptor-mediated calcium release resets synaptic homeostasis in presymptomatic 3xTg-AD mice. *J. Neurosci.* **29**, 9458–9470 (2009). doi: [10.1523/JNEUROSCI.2047-09.2009](https://doi.org/10.1523/JNEUROSCI.2047-09.2009); pmid: [19641109](https://pubmed.ncbi.nlm.nih.gov/19641109/)
18. E. K. Webber, M. Fivaz, G. E. Stutzmann, G. Griffioen, Cytosolic calcium: Judge, jury and executioner of neurodegeneration in Alzheimer’s disease and beyond. *Alzheimers Dement.* **19**, 3701–3717 (2023). doi: [10.1002/alz.13065](https://doi.org/10.1002/alz.13065); pmid: [37132525](https://pubmed.ncbi.nlm.nih.gov/37132525/)
19. S. I. Mota, I. L. Ferreira, A. C. Rego, Dysfunctional synapse in Alzheimer’s disease - A focus on NMDA receptors. *Neuropharmacology* **76**, 16–26 (2014). doi: [10.1016/j.neuropharm.2013.08.013](https://doi.org/10.1016/j.neuropharm.2013.08.013); pmid: [23973316](https://pubmed.ncbi.nlm.nih.gov/23973316/)
20. T. S. Anekonda *et al.*, L-type voltage-gated calcium channel blockade with isradipine as a therapeutic strategy for Alzheimer’s disease. *Neurobiol. Dis.* **41**, 62–70 (2011). doi: [10.1016/j.nbd.2010.08.020](https://doi.org/10.1016/j.nbd.2010.08.020); pmid: [20816785](https://pubmed.ncbi.nlm.nih.gov/20816785/)
21. M. Calvo-Rodriguez *et al.*, Increased mitochondrial calcium levels associated with neuronal death in a mouse model of Alzheimer’s disease. *Nat. Commun.* **11**, 2146 (2020). doi: [10.1038/s41467-020-16074-2](https://doi.org/10.1038/s41467-020-16074-2); pmid: [32358564](https://pubmed.ncbi.nlm.nih.gov/32358564/)
22. K.-H. Cheung *et al.*, Mechanism of Ca²⁺ disruption in Alzheimer’s disease by presenilin regulation of InsP₃ receptor channel gating. *Neuron* **58**, 871–883 (2008). doi: [10.1016/j.neuron.2008.04.015](https://doi.org/10.1016/j.neuron.2008.04.015); pmid: [18579078](https://pubmed.ncbi.nlm.nih.gov/18579078/)

23. J. Ye *et al.*, Tau-induced upregulation of C/EBP β -TRPC1-SOCE signaling aggravates tauopathies: A vicious cycle in Alzheimer neurodegeneration. *Aging Cell* **19**, e13209 (2020). doi: [10.1111/ace1.13209](https://doi.org/10.1111/ace1.13209); pmid: [32815315](https://pubmed.ncbi.nlm.nih.gov/32815315/)
24. Z. Sun *et al.*, SOCE-mediated NFAT1-NOX2-NLRP1 inflammasome involves in lipopolysaccharide-induced neuronal damage and A β generation. *Mol. Neurobiol.* **59**, 3183–3205 (2022). doi: [10.1007/s12035-021-02717-y](https://doi.org/10.1007/s12035-021-02717-y); pmid: [35286582](https://pubmed.ncbi.nlm.nih.gov/35286582/)
25. M. Dumbacher *et al.*, Modifying Rap1-signalling by targeting Pde6 δ is neuroprotective in models of Alzheimer's disease. *Mol. Neurodegener.* **13**, 50 (2018). doi: [10.1186/s13024-018-0283-3](https://doi.org/10.1186/s13024-018-0283-3); pmid: [30257685](https://pubmed.ncbi.nlm.nih.gov/30257685/)
26. J. Götz, G. Halliday, R. M. Nisbet, Molecular pathogenesis of the tauopathies. *Annu. Rev. Pathol.* **14**, 239–261 (2019). doi: [10.1146/annurev-pathmechdis-012418-012936](https://doi.org/10.1146/annurev-pathmechdis-012418-012936); pmid: [30355155](https://pubmed.ncbi.nlm.nih.gov/30355155/)
27. G. A. Krafft, W. L. Klein, ADDLs and the signaling web that leads to Alzheimer's disease. *Neuropharmacology* **59**, 230–242 (2010). doi: [10.1016/j.neuropharm.2010.07.012](https://doi.org/10.1016/j.neuropharm.2010.07.012); pmid: [20650286](https://pubmed.ncbi.nlm.nih.gov/20650286/)
28. G. Fani *et al.*, A β oligomers dysregulate calcium homeostasis by mechanosensitive activation of AMPA and NMDA receptors. *ACS Chem. Neurosci.* **12**, 766–781 (2021). doi: [10.1021/acscchemneuro.0c00811](https://doi.org/10.1021/acscchemneuro.0c00811); pmid: [33538575](https://pubmed.ncbi.nlm.nih.gov/33538575/)
29. F. G. De Felice *et al.*, Alzheimer's disease-type neuronal tau hyperphosphorylation induced by A beta oligomers. *Neurobiol. Aging* **29**, 1334–1347 (2008). doi: [10.1016/j.neurobiolaging.2007.02.029](https://doi.org/10.1016/j.neurobiolaging.2007.02.029); pmid: [17403556](https://pubmed.ncbi.nlm.nih.gov/17403556/)
30. M. Caligiuri *et al.*, MASP1: Three-hybrid trap for quantitative proteome fingerprinting of small molecule-protein interactions in mammalian cells. *Chem. Biol.* **13**, 711–722 (2006). doi: [10.1016/j.chembiol.2006.05.008](https://doi.org/10.1016/j.chembiol.2006.05.008); pmid: [16873019](https://pubmed.ncbi.nlm.nih.gov/16873019/)
31. A. A. Bridges, A. S. Gladfelter, Septin form and function at the cell cortex. *J. Biol. Chem.* **290**, 17173–17180 (2015). doi: [10.1074/jbc.R114.634444](https://doi.org/10.1074/jbc.R114.634444); pmid: [25957401](https://pubmed.ncbi.nlm.nih.gov/25957401/)
32. S. Mostowy, P. Cossart, Septins: The fourth component of the cytoskeleton. *Nat. Rev. Mol. Cell Biol.* **13**, 183–194 (2012). doi: [10.1038/nrm3284](https://doi.org/10.1038/nrm3284); pmid: [22314400](https://pubmed.ncbi.nlm.nih.gov/22314400/)
33. J. R. Bowen, D. Hwang, X. Bai, D. Roy, E. T. Spiliotis, Septin GTPases spatially guide microtubule organization and plus end dynamics in polarizing epithelia. *J. Cell Biol.* **194**, 187–197 (2011). doi: [10.1083/jcb.201102076](https://doi.org/10.1083/jcb.201102076); pmid: [21788367](https://pubmed.ncbi.nlm.nih.gov/21788367/)
34. A. Kinoshita *et al.*, Identification of septins in neurofibrillary tangles in Alzheimer's disease. *Am. J. Pathol.* **153**, 1551–1560 (1998). doi: [10.1016/S0002-9440\(10\)65743-4](https://doi.org/10.1016/S0002-9440(10)65743-4); pmid: [9811347](https://pubmed.ncbi.nlm.nih.gov/9811347/)
35. M. E. Pedersen, J. Østergaard, H. Jensen, Flow-induced dispersion analysis (FIDA) for protein quantification and characterization. *Methods Mol. Biol.* **1972**, 109–123 (2019). doi: [10.1007/978-1-4939-9213-8_8](https://doi.org/10.1007/978-1-4939-9213-8_8); pmid: [30847787](https://pubmed.ncbi.nlm.nih.gov/30847787/)
36. M. Kinoshita, C. M. Field, M. L. Coughlin, A. F. Straight, T. J. Mitchison, Self- and actin-templated assembly of Mammalian septins. *Dev. Cell* **3**, 791–802 (2002). doi: [10.1016/S1534-5807\(02\)00366-0](https://doi.org/10.1016/S1534-5807(02)00366-0); pmid: [12479805](https://pubmed.ncbi.nlm.nih.gov/12479805/)
37. S. Sharma *et al.*, An siRNA screen for NFAT activation identifies septins as coordinators of store-operated Ca²⁺ entry. *Nature* **499**, 238–242 (2013). doi: [10.1038/nature12229](https://doi.org/10.1038/nature12229); pmid: [23792561](https://pubmed.ncbi.nlm.nih.gov/23792561/)
38. B. K. Deb, T. Pathak, G. Hasan, Store-independent modulation of Ca(2+) entry through Orai by Septin 7. *Nat. Commun.* **7**, 11751 (2016). doi: [10.1038/ncomms11751](https://doi.org/10.1038/ncomms11751); pmid: [27225060](https://pubmed.ncbi.nlm.nih.gov/27225060/)
39. X. Liang, N. Zhang, H. Pan, J. Xie, W. Han, Development of store-operated calcium entry-targeted compounds in cancer. *Front. Pharmacol.* **12**, 688244 (2021). doi: [10.3389/fphar.2021.688244](https://doi.org/10.3389/fphar.2021.688244); pmid: [34122115](https://pubmed.ncbi.nlm.nih.gov/34122115/)
40. Q. Hu, W. J. Nelson, E. T. Spiliotis, Forchlorfenuron alters mammalian septin assembly, organization, and dynamics. *J. Biol. Chem.* **283**, 29563–29571 (2008). doi: [10.1074/jbc.M804962200](https://doi.org/10.1074/jbc.M804962200); pmid: [18713753](https://pubmed.ncbi.nlm.nih.gov/18713753/)
41. F. Vallesse *et al.*, An expanded palette of improved SPLICS reporters detects multiple organelle contacts in vitro and in vivo. *Nat. Commun.* **11**, 6069 (2020). doi: [10.1038/s41467-020-19892-6](https://doi.org/10.1038/s41467-020-19892-6); pmid: [33247103](https://pubmed.ncbi.nlm.nih.gov/33247103/)
42. K. V. Kuchibhotla *et al.*, Abeta plaques lead to aberrant regulation of calcium homeostasis in vivo resulting in structural and functional disruption of neuronal networks. *Neuron* **59**, 214–225 (2008). doi: [10.1016/j.neuron.2008.06.008](https://doi.org/10.1016/j.neuron.2008.06.008); pmid: [18667150](https://pubmed.ncbi.nlm.nih.gov/18667150/)
43. Y. Yin *et al.*, Tau accumulation induces synaptic impairment and memory deficit by calcineurin-mediated inactivation of nuclear CaMKIV/CREB signaling. *Proc. Natl. Acad. Sci. U.S.A.* **113**, E3773–E3781 (2016). doi: [10.1073/pnas.1604519113](https://doi.org/10.1073/pnas.1604519113); pmid: [27298345](https://pubmed.ncbi.nlm.nih.gov/27298345/)
44. Y. Miao, A. Bhattarai, J. Wang, Ligand gaussian accelerated molecular dynamics (LiGaMD): Characterization of ligand binding thermodynamics and kinetics. *J. Chem. Theory Comput.* **16**, 5526–5547 (2020). doi: [10.1021/acs.jctc.0c00395](https://doi.org/10.1021/acs.jctc.0c00395); pmid: [32692556](https://pubmed.ncbi.nlm.nih.gov/32692556/)
45. D. C. Mendonça *et al.*, An atomic model for the human septin hexamer by cryo-EM. *J. Mol. Biol.* **433**, 167096 (2021). doi: [10.1016/j.jmb.2021.167096](https://doi.org/10.1016/j.jmb.2021.167096); pmid: [34116125](https://pubmed.ncbi.nlm.nih.gov/34116125/)
46. J. Jumper *et al.*, Highly accurate protein structure prediction with AlphaFold. *Nature* **596**, 583–589 (2021). doi: [10.1038/s41586-021-03819-2](https://doi.org/10.1038/s41586-021-03819-2); pmid: [34265844](https://pubmed.ncbi.nlm.nih.gov/34265844/)
47. H. V. D. Rosa *et al.*, Molecular recognition at septin interfaces: The switches hold the key. *J. Mol. Biol.* **432**, 5784–5801 (2020). doi: [10.1016/j.jmb.2020.09.001](https://doi.org/10.1016/j.jmb.2020.09.001); pmid: [32910969](https://pubmed.ncbi.nlm.nih.gov/32910969/)
48. M. Mendoza, A. A. Hyman, M. Glotzer, GTP binding induces filament assembly of a recombinant septin. *Curr. Biol.* **12**, 1858–1863 (2002). doi: [10.1016/S0960-9822\(02\)01258-7](https://doi.org/10.1016/S0960-9822(02)01258-7); pmid: [12419187](https://pubmed.ncbi.nlm.nih.gov/12419187/)
49. H. Takeuchi *et al.*, P301S mutant human tau transgenic mice manifest early symptoms of human tauopathies with dementia and altered sensorimotor gating. *PLOS ONE* **6**, e21050 (2011). doi: [10.1371/journal.pone.0021050](https://doi.org/10.1371/journal.pone.0021050); pmid: [21698260](https://pubmed.ncbi.nlm.nih.gov/21698260/)
50. A. H. Al-Nuaimi *et al.*, Robust EEG based biomarkers to detect Alzheimer's disease. *Brain Sci.* **11**, 1026 (2021). doi: [10.3390/brainsci11081026](https://doi.org/10.3390/brainsci11081026); pmid: [34439645](https://pubmed.ncbi.nlm.nih.gov/34439645/)
51. C. Babillon *et al.*, Measures of resting state EEG rhythms for clinical trials in Alzheimer's disease: Recommendations of an expert panel. *Alzheimers Dement.* **17**, 1528–1553 (2021). doi: [10.1002/alz.12311](https://doi.org/10.1002/alz.12311); pmid: [33860614](https://pubmed.ncbi.nlm.nih.gov/33860614/)
52. S. Daumas *et al.*, Faster forgetting contributes to impaired spatial memory in the PDAPP mouse: Deficit in memory retrieval associated with increased sensitivity to interference? *Learn. Mem.* **15**, 625–632 (2008). doi: [10.1101/lm.990208](https://doi.org/10.1101/lm.990208); pmid: [18772249](https://pubmed.ncbi.nlm.nih.gov/18772249/)
53. P. Li *et al.*, Memantine ameliorates cognitive deficit in AD mice via enhancement of entorhinal-CA1 projection. *BMC Neurosci.* **22**, 41 (2021). doi: [10.1186/s12868-021-00647-y](https://doi.org/10.1186/s12868-021-00647-y); pmid: [34120588](https://pubmed.ncbi.nlm.nih.gov/34120588/)
54. D. Xia *et al.*, Novel App knock-in mouse model shows key features of amyloid pathology and reveals profound metabolic dysregulation of microglia. *Mol. Neurodegener.* **17**, 41 (2022). doi: [10.1186/s13024-022-00547-7](https://doi.org/10.1186/s13024-022-00547-7); pmid: [35690868](https://pubmed.ncbi.nlm.nih.gov/35690868/)
55. J. McDaid, S. Mustaly-Kalimi, G. E. Stutzmann, Ca²⁺ dyshomeostasis disrupts neuronal and synaptic function in Alzheimer's disease. *Cells* **9**, 2655 (2020). doi: [10.3390/cells9122655](https://doi.org/10.3390/cells9122655); pmid: [33321866](https://pubmed.ncbi.nlm.nih.gov/33321866/)
56. M. A. O'Neal, N. R. Stallings, J. S. Malter, Alzheimer's disease, dendritic spines, and calcineurin inhibitors: A new approach? *ACS Chem. Neurosci.* **9**, 1233–1234 (2018). doi: [10.1021/acscchemneuro.8b00213](https://doi.org/10.1021/acscchemneuro.8b00213); pmid: [29757603](https://pubmed.ncbi.nlm.nih.gov/29757603/)
57. R. Prasherberger *et al.*, Neuronal identity defines α -synuclein and tau toxicity. *Neuron* **111**, 1577–1590.e11 (2023). doi: [10.1016/j.neuron.2023.02.033](https://doi.org/10.1016/j.neuron.2023.02.033); pmid: [36948206](https://pubmed.ncbi.nlm.nih.gov/36948206/)
58. M. A. Busche, B. T. Hyman, Synergy between amyloid- β and tau in Alzheimer's disease. *Nat. Neurosci.* **23**, 1183–1193 (2020). doi: [10.1038/s41593-020-0687-6](https://doi.org/10.1038/s41593-020-0687-6); pmid: [32778792](https://pubmed.ncbi.nlm.nih.gov/32778792/)
59. L. M. Ittner *et al.*, Dendritic function of tau mediates amyloid- β toxicity in Alzheimer's disease mouse models. *Cell* **142**, 387–397 (2010). doi: [10.1016/j.cell.2010.06.036](https://doi.org/10.1016/j.cell.2010.06.036); pmid: [20655099](https://pubmed.ncbi.nlm.nih.gov/20655099/)
60. B. K. Deb, P. Chakraborty, R. Gopurapilly, G. Hasan, SEPT7 regulates Ca²⁺ entry through Orai channels in human neural progenitor cells and neurons. *Cell Calcium* **90**, 102252 (2020). doi: [10.1016/j.ceca.2020.102252](https://doi.org/10.1016/j.ceca.2020.102252); pmid: [32682163](https://pubmed.ncbi.nlm.nih.gov/32682163/)
61. B. K. Deb, G. Hasan, SEPT7-mediated regulation of Ca²⁺ entry through Orai channels requires other septin subunits. *Cytoskeleton* **76**, 104–114 (2019). doi: [10.1002/cm.21476](https://doi.org/10.1002/cm.21476); pmid: [30004181](https://pubmed.ncbi.nlm.nih.gov/30004181/)
62. M. Ihara *et al.*, Association of the cytoskeletal GTP-binding protein Sept4/H5 with cytoplasmic inclusions found in Parkinson's disease and other synucleinopathies. *J. Biol. Chem.* **278**, 24095–24102 (2003). doi: [10.1074/jbc.M301352200](https://doi.org/10.1074/jbc.M301352200); pmid: [12695511](https://pubmed.ncbi.nlm.nih.gov/12695511/)
63. Y. M. Gozal *et al.*, Aberrant septin II is associated with sporadic frontotemporal lobar degeneration. *Mol. Neurodegener.* **6**, 82 (2011). doi: [10.1186/1750-1326-6-82](https://doi.org/10.1186/1750-1326-6-82); pmid: [22126117](https://pubmed.ncbi.nlm.nih.gov/22126117/)
64. JupyterLab notebooks for: K. Princen, T. Van Dooren, M. van Gorsel, N. Louros, X. Yang, M. Dumbacher, I. Bastiaens, K. Coupet, S. Dupont, E. Cuveliers, A. Lauwers, M. Laghmouchi, T. Vanwelden, S. Carmans, N. Van Damme, H. Duhamel, S. Vansteenkiste, J. Prerad, K. Pipeleers, O. Rodiers, L. De Ridder, S. Claes, Y. Busschots, L. Pringels, V. Verhelst, E. Debrux, M. Brouwer, S. Lievens, J. Tavernier, M. Farinelli, S. Hughes-Asceri, M. Voets, J. Winderickx, S. Wera, J. de Wit, J. Schymkowitz, F. Rousseau, H. Zetterberg, J. L. Cummings, W. Annaert, T. Cornelissen, H. De Winter, K. De Witte, M. Fivaz, G. Griffioen, Pharmacological modulation of septins restores calcium homeostasis and is neuroprotective in models of Alzheimer's disease. *Zenodo* (2024); doi: [10.5281/zenodo.10908219](https://doi.org/10.5281/zenodo.10908219)
65. Datasets for: K. Princen, T. Van Dooren, M. van Gorsel, N. Louros, X. Yang, M. Dumbacher, I. Bastiaens, K. Coupet, S. Dupont, E. Cuveliers, A. Lauwers, M. Laghmouchi, T. Vanwelden, S. Carmans, N. Van Damme, H. Duhamel, S. Vansteenkiste, J. Prerad, K. Pipeleers, O. Rodiers, L. De Ridder, S. Claes, Y. Busschots, L. Pringels, V. Verhelst, E. Debrux, M. Brouwer, S. Lievens, J. Tavernier, M. Farinelli, S. Hughes-Asceri, M. Voets, J. Winderickx, S. Wera, J. de Wit, J. Schymkowitz, F. Rousseau, H. Zetterberg, J. L. Cummings, W. Annaert, T. Cornelissen, H. De Winter, K. De Witte, M. Fivaz, G. Griffioen, Pharmacological modulation of septins restores calcium homeostasis and is neuroprotective in models of Alzheimer's disease. *Zenodo* (2024); doi: [10.5281/zenodo.10908261](https://doi.org/10.5281/zenodo.10908261)
66. Matlab codes for: K. Princen, T. Van Dooren, M. van Gorsel, N. Louros, X. Yang, M. Dumbacher, I. Bastiaens, K. Coupet, S. Dupont, E. Cuveliers, A. Lauwers, M. Laghmouchi, T. Vanwelden, S. Carmans, N. Van Damme, H. Duhamel, S. Vansteenkiste, J. Prerad, K. Pipeleers, O. Rodiers, L. De Ridder, S. Claes, Y. Busschots, L. Pringels, V. Verhelst, E. Debrux, M. Brouwer, S. Lievens, J. Tavernier, M. Farinelli, S. Hughes-Asceri, M. Voets, J. Winderickx, S. Wera, J. de Wit, J. Schymkowitz, F. Rousseau, H. Zetterberg, J. L. Cummings, W. Annaert, T. Cornelissen, H. De Winter, K. De Witte, M. Fivaz, G. Griffioen, Pharmacological modulation of septins restores calcium homeostasis and is neuroprotective in models of Alzheimer's disease. *Zenodo* (2024); doi: [10.5281/zenodo.10908299](https://doi.org/10.5281/zenodo.10908299)

ACKNOWLEDGMENTS

We thank K. Sahni Ray, M. Albasini, and H. Jensen (Fidabio) for expertise and guidance in all FIDA experiments; B. de Strooper for scientific advice; P. Verstreken, G. Halder, and B. Verpoort for critical reading of the manuscript; and the Bioimaging Core (VIB, Leuven) for training, technical support, and access to the instrument park. **Funding:** reMYND is supported by Flanders Innovation & Entrepreneurship (VLAIO), formerly known as the Institute for the Promotion of Innovation by Science and Technology, in Flanders (grants 030383, 070157, 080394, and 090494 to G.G. and VLAIO ICON grant HBC.2019.2523 to T.C.). The Switch lab is supported by the Flanders Institute of Biotechnology (VIB grant C0401 to F.R. and J.S.), the Fund for Scientific Research Flanders (FWO postdoctoral fellowships 12P0919N and 12P0922N to N.L.), and Stichting Alzheimer Onderzoek/Fondation Recherche Alzheimer (SAO-FRA grant 2022/0020 to N.L.). The Laboratory for Membrane Trafficking is supported by VIB KU Leuven (grants C14/21/095 and SMINF KA/20/085 to W.A.), FWO (project grants G078117N, G056017N, G0C4220N, and I001322N to W.A.), SAO-FRA (grants 2020/030 and 2022/022 to W.A. and postdoctoral fellowship 12E0123N to X.Y.), and the Alzheimer's Association (grant AARF-22-968022 to X.Y.). The Laboratory of Synapse Biology is supported by SAO-FRA (grant 2019/0013 to J.D.W.), FWO (project grants G0C4518N, G0A8720N, and G0A8320N to J.D.W.), FWO EOS (grant G0H2818N to J.D.W.), ERANET-NEURON TAO2PATHY (grant G0I3118N to J.D.W.), KU Leuven/Flemish Government (Methusalem Grant to J.D.W.), and NWO (Rubicon grant 452020222 to M.B.). The Cytokine Receptor Lab is supported by Ugent (Methusalem grant to J.T.). J.L.C. is supported by the National Institutes of Health [National Institute of General Medical Sciences (NIGMS) grant P20GM109025, National Institute of Neurological Disorders and Stroke (NINDS) grant U01NS093334, and National Institute on Aging (NIA) grants R01AG053798, P30AG072959, R35AG7476, and R25 AG083721-01], the Alzheimer's Drug Discovery Foundation (ADDF), the Ted and Maria Quirk Endowment, and the Joy Chambers-Grundy Endowment. H.Z. is supported by the Swedish Research Council (grants 2023-00356, 2022-01018, and 2019-02397), the European Union's Horizon Europe Research and Innovation Program (grant 101053962), Swedish State Support for Clinical Research (grant ALFGBG-71320), ADDF (grant 201809-2016862), the AD Strategic Fund and the Alzheimer's Association (grants ADSF-21-831376-C, ADSF-21-831381-C, ADSF-21-831377-C, and ADSF-24-1284328-C), the Bluefield Project, the Cure Alzheimer's Fund, the Olaf Thon Foundation, the Erling-Persson Family Foundation, Familien Rönströms Stiftelse, Stiftelsen för Gamla Tjänarinnor (grant F02022-0270), the European Union's Horizon 2020 Research and

Innovation Program (Marie Skłodowska-Curie grant 860197 MIRIADÉ), the European Union Joint Programme–Neurodegenerative Disease Research (grant JPND2021-00694), the National Institute for Health and Care Research University College London Hospitals Biomedical Research Centre, and the UK Dementia Research Institute at UCL (grant UKDRI-1003).

Author contributions: Conceptualization: G.G., K.Pr., T.V.D., M.Fi.; Funding acquisition: K.D.W., G.G.; Investigation: K.Pr., T.V.D., M.v.G., N.L., X.Y., S.L., J.T., M.V., J.W., J.S., F.R., J.d.W., W.A., S.W., M.Fi., G.G.; Methodology: K.Pr., T.V.D., M.v.G., N.L., X.Y., M.D., I.B., K.C., S.D., E.C., A.L., M.L., T.V., S.Ca., N.V.D., H.D., S.V., J.P., K.Pi., O.R., L.D.R., S.Cl., Y.B., M.B., S.L., J.T., M.Fa., S.H.-A., M.V., J.W., S.W., J.S., F.R., J.d.W., W.A., T.C., H.D.W., M.Fi., G.G.; Project administration: K.Pr., T.V.D., L.P., V.V., E.D., K.D.W., M.Fi., G.G.; Supervision: G.G., K.Pr., T.V.D., V.V., L.P., H.D.W., J.S., F.R., W.A., T.C., M.Fi.; Writing – original draft: M.Fi., G.G.; Writing – review and editing: M.Fi., G.G., M.v.G., H.Z., J.L.C. **Competing interests:** H.Z. has served at scientific advisory boards and/or as a consultant for Abbvie, Acumen, Alector, Alzinova, ALZPath, Amylyx, Annexon, Apellis, Artery Therapeutics, AZTherapies, Cognito Therapeutics, CogRx, Denali, Eisai, Merry Life, Nervgen, Novo Nordisk, Optoceutics, Passage Bio, Pinteon Therapeutics, Prothena, Red Abbey Labs, reMYND, Roche, Samumed, Siemens Healthineers, Triplet Therapeutics, and Wave; has given lectures in

symposia sponsored by Alzecure, Biogen, Cellectricon, Fujirebio, Lilly, Novo Nordisk, and Roche; and is a cofounder of Brain Biomarker Solutions in Gothenburg AB (BBS), which is a part of the GU Ventures Incubator Program (outside submitted work). J.L.C. has provided consultation to Acadia, Actinogen, Acumen, AlphaCognition, ALZpath, Aprinoia, AriBio, Artery, Biogen, Biohaven, BioVie, BioXcel, Bristol-Myers Squibb, Cassava, Cerecin, Diadem, Eisai, GAP Foundation, GemVax, Janssen, Jocasta, Karuna, Lighthouse, Lilly, Lundbeck, LSP/eqt, Merck, NervGen, New Amsterdam, Novo Nordisk, Oligomerix, Optoceutics, Ono, Otsuka, Oxford Brain Diagnostics, Prothena, reMYND, Roche, Sage Therapeutics, Signant Health, Simcere, Sinaptica, Suven, TrueBinding, Vaxxinity, and Wren pharmaceutical, assessment, and investment companies. J.W. and S.W. are cofounders and shareholders of reMYND. G.G. is a consultant for reMYND and owns reMYND warrants and shares. M.Fi. owns reMYND warrants. J.d.W. is cofounder of Augustine Tx and served as scientific advisory board member for Augustine Tx. J.T. is cofounder of Orionis Biosciences. K.Pr. and G.G. are inventors on patent WO2013/004642 held by reMYND NV: "1,2,4-thiadiazol-5-ylpiperazine derivatives useful in the treatment of neurodegenerative diseases." K.Pr., M.V., M.Fi., and G.G. are inventors on patent application EP23209465.6 submitted by reMYND NV: "Modulators of septin 6 for use in the prevention and/or treatment of neurodegenerative disorders." **Data and**

materials availability: The tauP301L BE(2)-M17 cell line and the ReS19-T compounds are available from G.G. under a material transfer agreement with reMYND. DNA plasmid sequences used in this study have been deposited in GenBank with accession numbers PP179526, PP179527, PP179528, PP179529, PP179530, and PP179531. JupyterLab notebooks (64), associated datasets (65) and Matlab codes (66) have been deposited on Zenodo.

License information: Copyright © 2024 the authors, some rights reserved; exclusive licensee American Association for the Advancement of Science. No claim to original US government works. <https://www.science.org/about/science-licenses-journal-article-reuse>

SUPPLEMENTARY MATERIALS

[science.org/doi/10.1126/science.add6260](https://doi.org/10.1126/science.add6260)

Materials and Methods

Figs. S1 to S11

Tables S1 to S7

References (67–75)

MDAR Reproducibility Checklist

Submitted 2 September 2022; resubmitted 19 November 2023

Accepted 4 April 2024

10.1126/science.add6260